A Review of Aeronautical Fatigue Investigations in Sweden During the Period April 2015 to March 2017

Edited by HANS ANSELL
Saab AB
Sweden

Saab Doc. No. LN-037309

Presented at the 35th Conference of the International Committee on Aeronautical Fatigue and Structural Integrity (ICAF), Nagoya, Japan, 5-6 June 2017.

CONTENT

1 INTRODUCTION

In this paper a review is given of the work carried out in Sweden in the area of aeronautical fatigue and structural integrity during the period April 2015 to March 2017. The review includes basic studies and industrial applications.

Contributions to the present review are from the following bodies:

- Saab AB
  Sections 2.1, 2.2, 2.3, 2.4, 2.5, 2.6, 2.7, 2.9, 2.10, 3.1

- Linkoping University (LiU)
  Sections 2.5, 2.7, 2.9, 2.10, 3.1

- The Royal Institute of Technology (KTH)
  Sections 3.2, 3.3

- Börje Andersson Research & Engineering AB (BARE)
  Sections 2.8

- Technical Research Centre of Finland (VTT)
  Sections 2.6

2 STRUCTURAL INTEGRITY CHARACTERISTICS OF METAL MATERIALS AND STRUCTURE

2.1 Damage tolerance test verification programme for Gripen E airframe

Hans Ansell, Zlatan Kapidžić, Martin Ekström, Saab AB

Service life and damage tolerance capability need to be verified by testing. These tests can either be based on similarities to previously conducted tests, if applicable, or by new tests when no previous test results are available. Full-scale testing is required when:

- Changed design principles in primary load paths
- Changed material in safety-of-flight critical parts
- Significant change of stress conditions in legacy primary load paths

When Gripen A/B was initially developed, the test verification task was huge since all of the above criteria applied. Especially the implementation of the damage tolerance task according to the MIL-A-83444 specification called for test verification. An extensive fatigue and damage tolerance test program of full-scale test assemblies was accomplished, see figure 2.1-1. Both airframe and systems parts, e.g. actuators in the flight control system, were included and a total of about 800 artificial defects, sizing between .05 and .25 inch, were introduced in the structural parts and in the correct structural surroundings. In addition conventional full-scale static and fatigue tests of both A and B versions were conducted covering testing beyond ultimate loads and 4 lifetimes respectively. More detailed description of this work can be found in [1] for airframe and [2] for mechanical system.

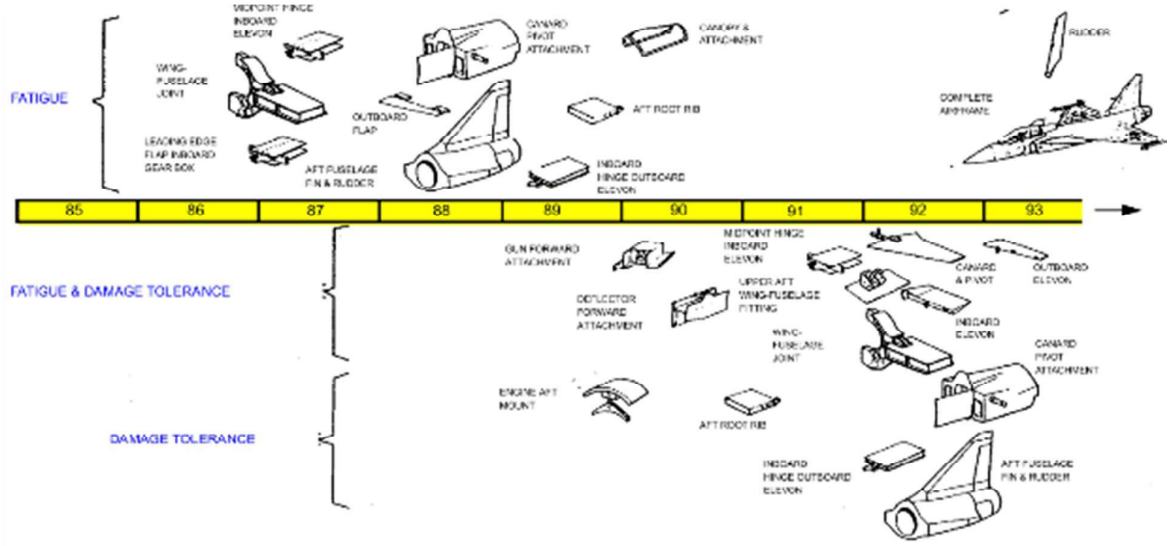

Figure 2.1-1. Test programme for fatigue and damage tolerance verification of Gripen A/B airframe.

When Gripen C/D was developed, no change of materials was done and no change of major load paths. Essential changes of local geometries were however done through the redesign to integral structures, extended service life (from 4,000 to 8,000 hours) and increased basic design mass (~10% compared to A/B versions) and some other load and structural changes, e.g. air-to-air refuelling probe, called for new full-scale fatigue tests, se figure 2.1-2. Damage tolerance tests were however not done in any large extent since the load path were the same although redesigned but the validation effort done on the fracture mechanic based damage tolerance methods during the A/B developments were deemed to be sufficient also for the C/D versions.

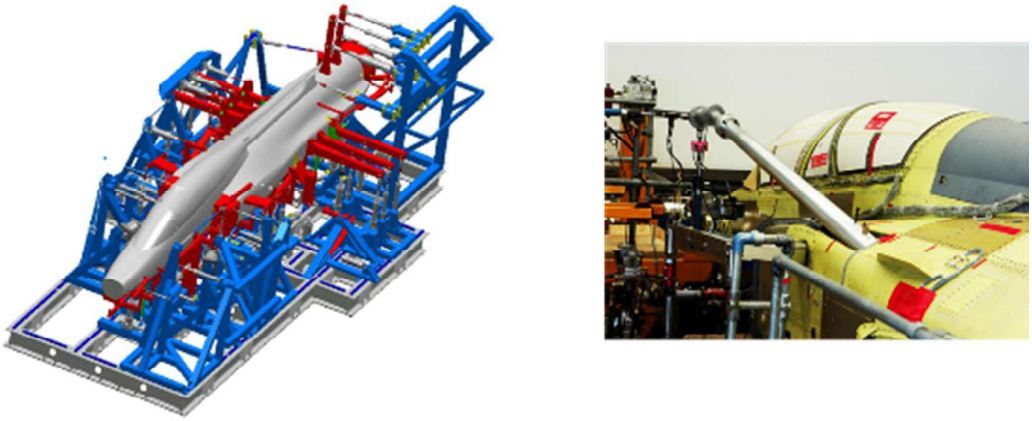

Figure 2.1-2. Full-scafe fatigue test of Gripen D version.

With the development of Gripen NG versions, structural changes were made that interrogated with several of the criteria for the need of test verification. Certification for airworthiness by full-scale testing required due to:

- New mid fuselage/wing design, fuselage joints, MLG attachments
- Change of classification of parts due to design-for-manufacturing purposes
- Use of a new material type (Al-Li AA2050 and AA2060)
- Increased basic design mass (~40% compared to C/D versions)
- New operational profiles

These structural changes call for a more extensive test programme than what was needed for the C/D versions. A full-scale static test (including impact damaged composite parts) of the complete airframe is underway and a full-scale fatigue test of the complete airframe will follow thereafter and tested in the same rig for 4 lifetimes, see figure 2.1-3. In addition to the full-scale fatigue test, control surfaces (not included in the test airframe) will be tested in separate assemblies. These tests will be a combined fatigue and damage tolerance test by initially cycled for 2 lifetimes without artificial initial defect followed by 2 lifetimes with artificially manufactured defects installed.

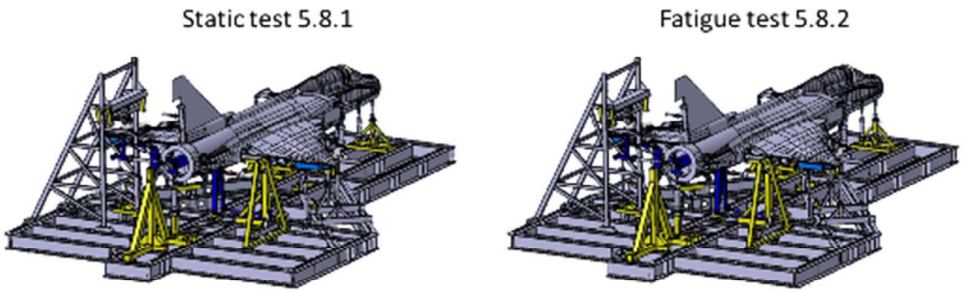

Figure 2.1-3. Full scale fatigue tests of Gripen E version.

Full-scale tests for compliance with damage tolerance requirements are also needed due to the structural changes in load paths and the upgraded classification of fuselage stringer joints and the design change of the wing to fuselage joint. A change from AA7050 alloy to AA2050 alloy in safety-of-flight critical parts also makes the damage tolerance test verification needed. The decision to use aluminium-lithium alloys in primary structural components was preceded by extensive validations of the fatigue and damage tolerance material properties. To assure necessary and sufficient confidence regarding damage tolerance, a significant test effort designed to challenge typical airframe crack scenarios with part through cracks (surface cracks in thickness steps, open and loaded holes etc.) was accomplished.

Figure 2.1-4 shows structural objects/assemblies which are verified for damage tolerance when having multiple artificial initial defects installed in critical sections.

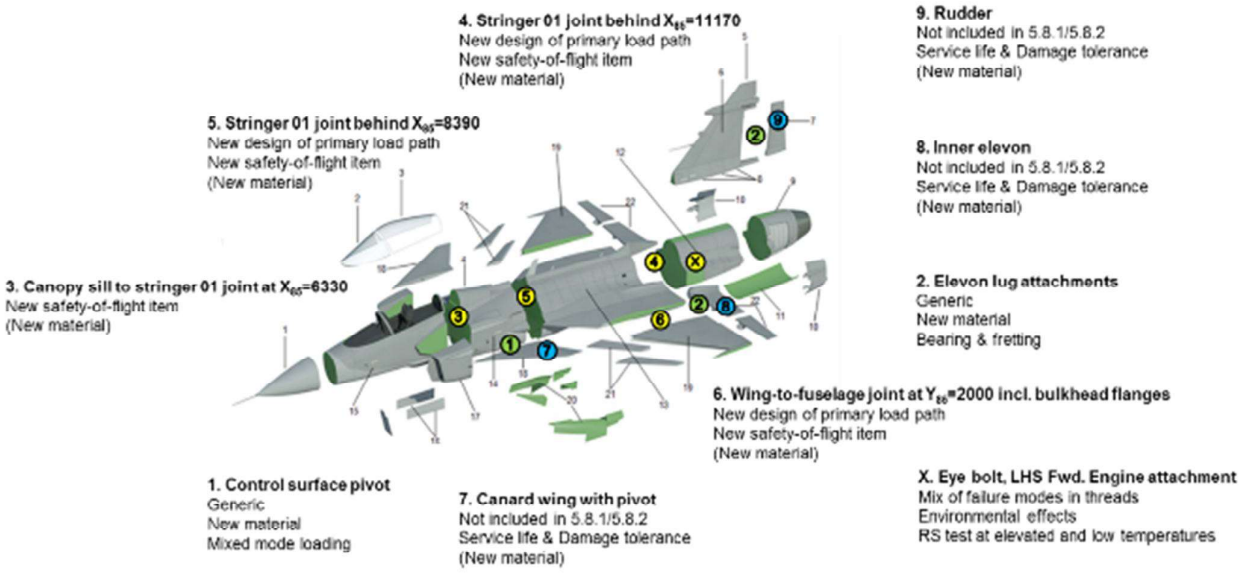

Figure 2.1-4. Full-scale damage tolerance tests of assemblies having artificial defects installed.

The component test “Canopy sill to stringer 01 joint at X_{85}=6330” is a certification test. The cause of test is upgraded criticality level + potential material change. Three test specimen will be will be used, both with and without artificially introduced defects.

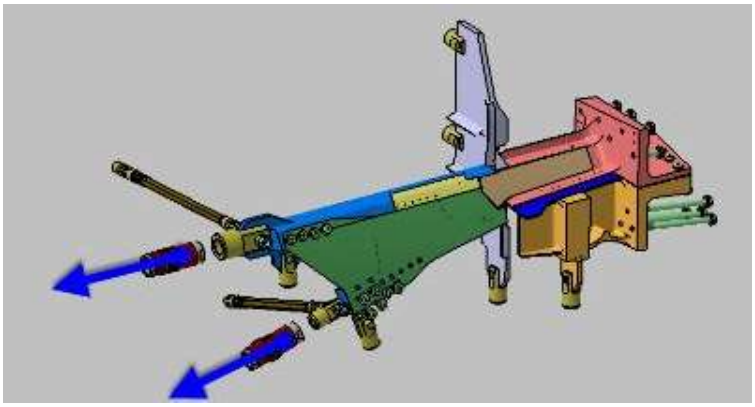

Figure 2.1-5. The component test “Canopy sill to stringer 01 joint at X_{85}=6330”.

The component test “Stringer 01 joint behind X_{85}=8390” is also a certification test. The cause of test is upgraded criticality level + potential material change. Three test specimen will be will be used, both with and without artificially introduced defects.

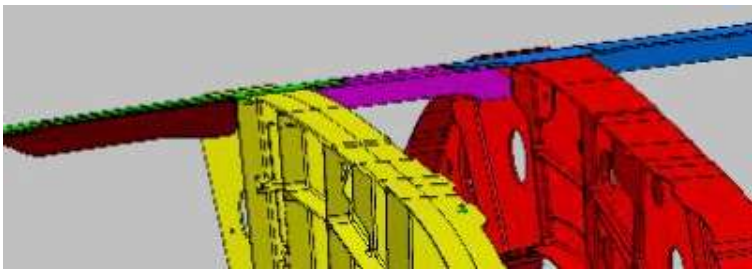

Figure 2.1-6. The component test “Stringer 01 joint behind X_{85}=8390”. The figure shows the design for the current area.

The component test “Wing to fuselage joint at Y_{85}=2000 incl. bulkhead flanges” is also a certification test. The cause of test is new design, upgraded criticality level and material change. One test specimen will be furnished with artificial defects.

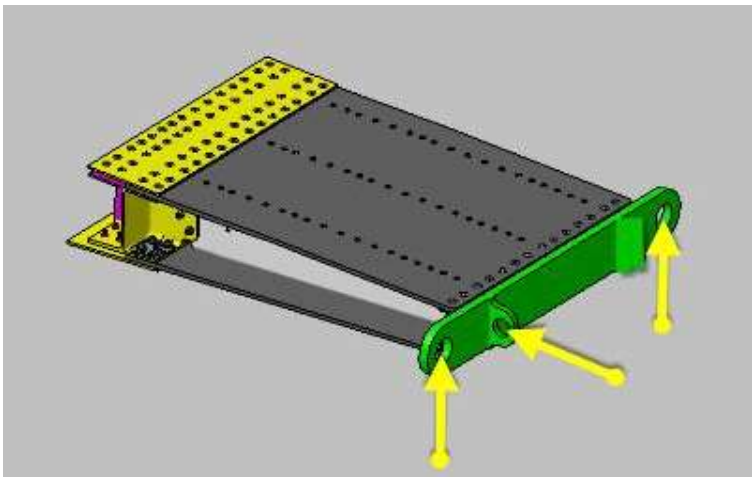

Figure 2.1-7. The component test “Wing to fuselage joint at Y_{85}=2000 incl. bulkhead flanges”. The figure shows the part of the test specimen outside the wing joint.

2.2 Full-scale static test of Gripen E airframe

Björn Fredriksson, Martin Ekström, Saab AB

A full-scale static test of the Gripen E single seater airframe is currently being conducted. The purposes of the test are to:

- Verify static strength of the airframe
- Verify stress analysis of new design concepts (FE-models)
- Airworthiness approval of first flying unit
- Fast opening of flight test envelop
- Reduce strain measurements on flight test aircraft

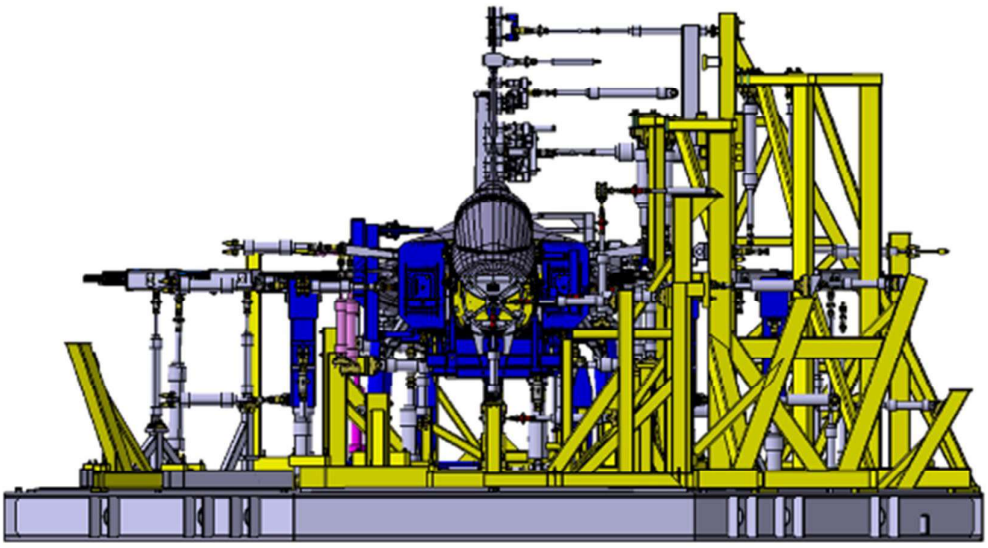

Figure 2.2-1 Static test set-up

The test objectives are categorized according to Overall, Primary and Secondary objectives, see sections below.

Overall objectives
The overall objectives with the test are to:

- Open the envelope for test aircraft 39.8.
- Verify the static strength requirements.
- Verify the stiffness / load distribution of the global FE-model.

Primary objectives
The primary objectives are to verify the static strength of:

- The wing and the wing joints at 180 % LL.
- The fuselage at 150 % LL.
- The fin and the fin attachment towards the fuselage at 180 % LL.

Secondary objectives

Secondary objectives are to:

- Verify the static strength of the attachments on the wing for the following components:
  - Inner and outer flap
  - Inner and outer elevon
  - Pylon 1 L/R, Pylon 2 L/R, Pylon 3 L/R

- Verify the attachments on the fuselage for the following components:
  - Radar attachment
  - AAR
  - NLG
  - MLG's
  - Canards
  - Air intakes
  - Pylon 4, Pylon 5 L/C/R
  - Engine

- Verify the rudder attachments on the fin.

The test object consists of an airframe representing the test aircraft with fuselage, wings and fin. Landing gears, control surfaces, weapon pylons, canards and engine are replaced by "dummies" and are tested separately.

The test is loaded by 126 load control channels for hydraulic actuators and 8 control channels for pressurized air in fuel tanks, cock-pit and air intakes and furnished with 2400 strain gauges for stress measurements.

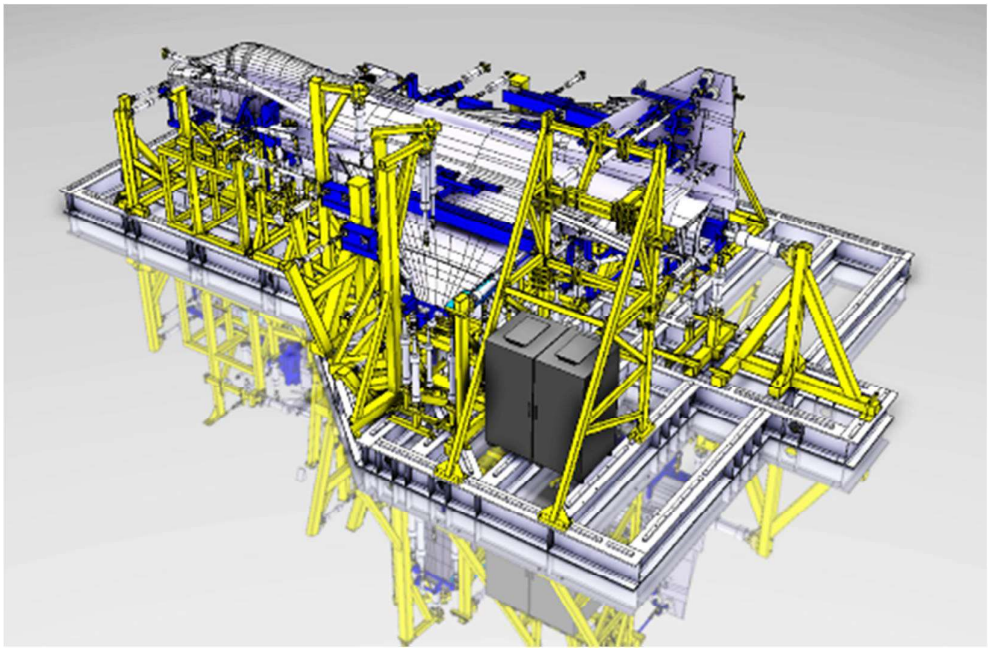

Figure 2.2-2. Static test setup, side view

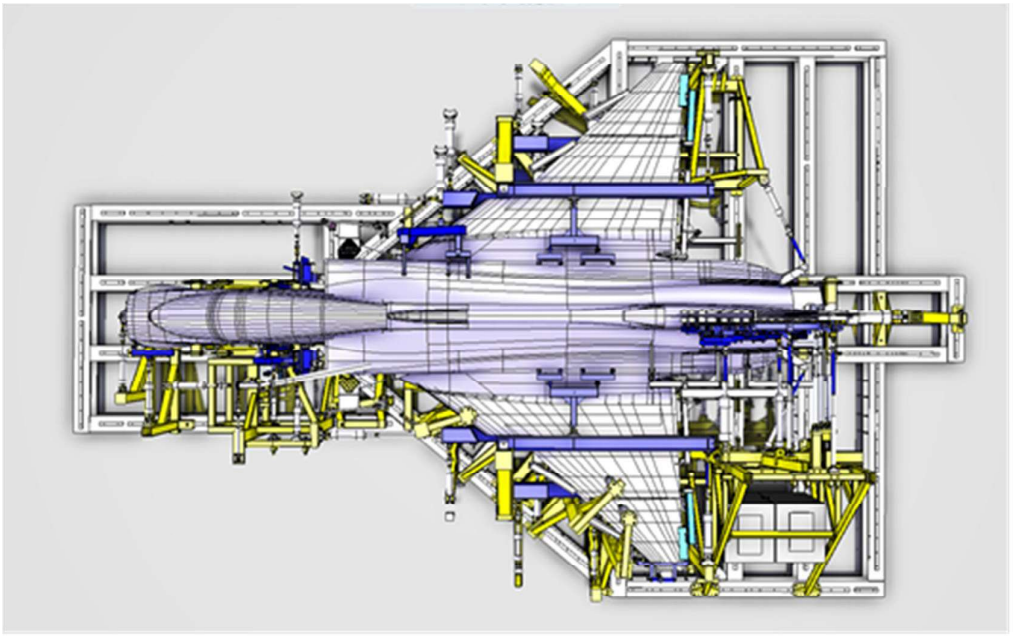

Figure 2.2-3. Static test set-up, top view

Figure 2.2-4. Static test during assembly of airframe in test rig, top view

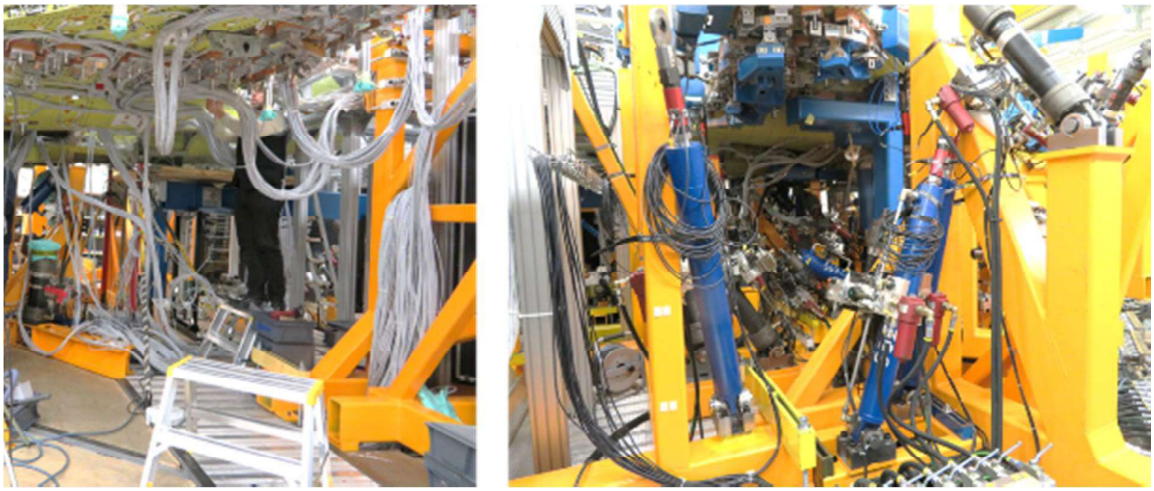

Figure 2.2-5 Static test during assembly of airframe in test rig, view from below

2.3 Method for computation of fatigue crack growth in lug joints

Zlatan Kapidžić, Hans Ansell, Saab AB

Lug joints are common structural elements in aircraft structures. Such joints are normally exposed to cyclic loading, often in a variable direction. There is therefore a risk of fatigue crack initiation and propagation in the areas with relatively high stresses. Because of that risk, damage tolerant dimensioning of critical lugs is performed where a sufficiently long time of slow crack growth is ensured. This is normally done by integration of crack growth rate as a function of the stress intensity factor range over the number of load cycles. In cracked lugs exposed to variable load directions, the stress intensity factor and thereby the crack growth rate varies with the load direction.

Currently used crack growth software AFGROW offers possibilities for computation of crack growth in lugs. However, only axially loaded, straight lugs, where the crack (corner crack or through crack) is placed in the perpendicular direction to the load direction, see Figure 2.3-1 left, are available. Effects of bushing interference on the crack growth life are not included. Generally, the use of structural lugs comprises both straight lugs and tapered lugs loaded in an arbitrary, and possibly varying, direction and considering a crack placed at an arbitrary location along the lughole edge. Moreover, the beneficial effect of interference bushings needs to be taken into account in order to produce reasonably accurate predictions of the crack growth life. The proposed method considers:

- Axially loaded straight lugs, with a through or a corner crack placed in the perpendicular direction to the load direction.
- Tapered lugs (taper angle = 22.5°), with a through or a corner crack placed at one of 16 possible locations around the lughole edge and loaded in a fix but arbitrary direction.
- User defined lug geometry.
- Effect of a given bushing interference on the crack growth in the two previous points.
- Constant amplitude or spectrum loading.

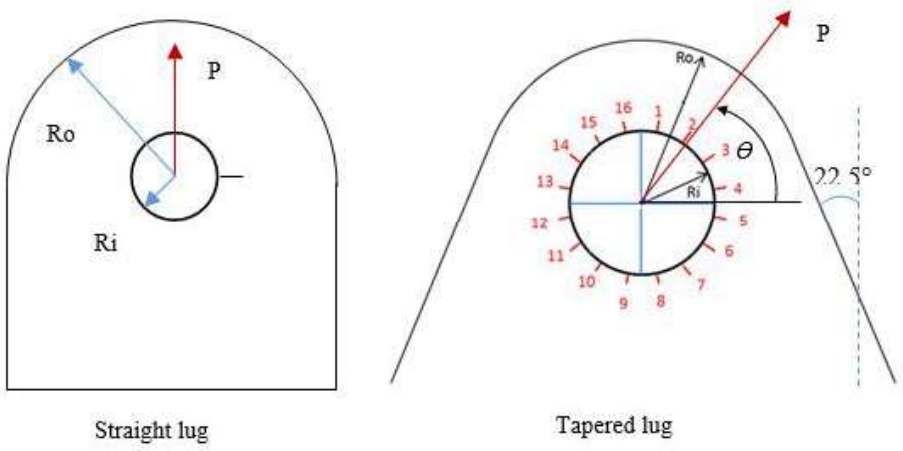

Figure 2.3-1. Lug geometry, load direction and crack position.

Computational procedure

The input data required by the method contains the information of the lug geometry (lug type (straight, tapered or user defined), hole diameter, width, thickness), the initial crack length and position, bearing load spectrum and direction, and material data (crack growth rate, fracture toughness etc.).

The crack growth calculation is performed incrementally for each spectrum block of cycles that have the same bearing stress maximum and minimum level and in the sequential order in which they appear in the spectrum. The spectrum is repeated until failure takes place according to residual strength failure criteria. The procedure is as follows:

For each block i of n number of cycles in the spectrum

- *Determine the bearing stress range $\Delta\sigma_b$ and the stress ratio R*
- *Compute the stress intensity factor ranges*

$$\Delta K_a = \Delta\sigma_b\sqrt{\pi a}\beta_a(a,c,D,W,t,\varphi,\theta)$$

$$\Delta K_c = \Delta\sigma_b\sqrt{\pi c}\beta_c(a,c,D,W,t,\varphi,\theta)$$

where β_c and β_a are the geometry functions for the surface crack of length c and for the through-the-thickness crack of length a respectively, which also depend on the load angle θ and the crack location angle φ. For straight, axially loaded lugs with a through crack or a corner crack, the closed form solutions from [1] are implemented. For lugs with a taper angle of 22.5°, a database containing FE-solutions of geometry functions for through cracks for a range of lug geometries, crack locations and load directions, is utilized. Geometry functions for through cracks for any other lug geometry can be supplied as a user defined input.

The corner crack solution is in all cases compounded from the through crack solution for the actual case and the ratio of the geometry functions for corner crack and through crack for an axially loaded straight lug. A corner crack becomes a straight front through crack either when a/t>0.95 or when β_c for the corner crack > β_c for the through crack.

The positive effect of interference bushing on the crack growth can be accounted for by correction of the stress intensity factor. The correction depends on the bushing dimensions, interference pressure *p* and the applied bearing load. The total stress intensity factor is assumed to have the following form

$$K = \sigma_b \sqrt{\pi c}\, \beta_L + p\sqrt{\pi c}\, \beta_p e^{-\gamma \sigma_b}$$

where the first term is the stress intensity factor for the crack in a lug without bushing and the second term represents the increase of the stress intensity factor due to the interference pressure. The geometry function β_p is derived [2] for a circular ring with a crack and γ is an experimentally derived parameter.

- *Compute the crack growth rates*

$$\frac{da}{dN} = f(\Delta K_a, R, ..)$$
$$\frac{dc}{dN} = f(\Delta K_c, R, ..)$$

where the function *f* is assumed to be according to the Forman-Newman-de Koning equation.

- *Update the crack lengths*

$$a_{i+1} = a_i + \left(\frac{da}{dN}\right)_i n$$
$$c_{i+1} = c_i + \left(\frac{dc}{dN}\right)_i n$$

If the crack growth increment c_{i+1} - c_i for a cycle block *i* is larger than a prescribed percentage of the current crack length c_i, the block is divided into halves and the calculation repeated until this criterion is fulfilled.

- *Check the failure criteria*

The failure takes place when any of the three criteria are met:

K_c>fracture toughness
Net-section stress>yield stress
c>0.9·net-section

- *Increase the number of cycles/flight hours*

$$N_{i+n} = N_i + n$$

Validation
The predictions of the current method are compared to tests performed on two cases:

- Straight lug loaded with constant amplitude axial load.
- Tapered lug loaded with a spectrum load in an inclined direction.

Straight lug, constant amplitude

Three constant amplitude tests were performed on lugs with a single corner crack and the surface crack length was measured continuously. Predictions were based on the following lug data and the results are shown in figure 2.3-2:

Applied load P = 75600 N, R = 0
Lug material: AA7010-T7451
Inner radius = 15.875 mm
Outer radius = 38.5 mm
Thickness = 20 mm
Bushing inner diameter = 27 mm
Bushing material: Steel
Measured bushing-lug interference = 0.042 mm

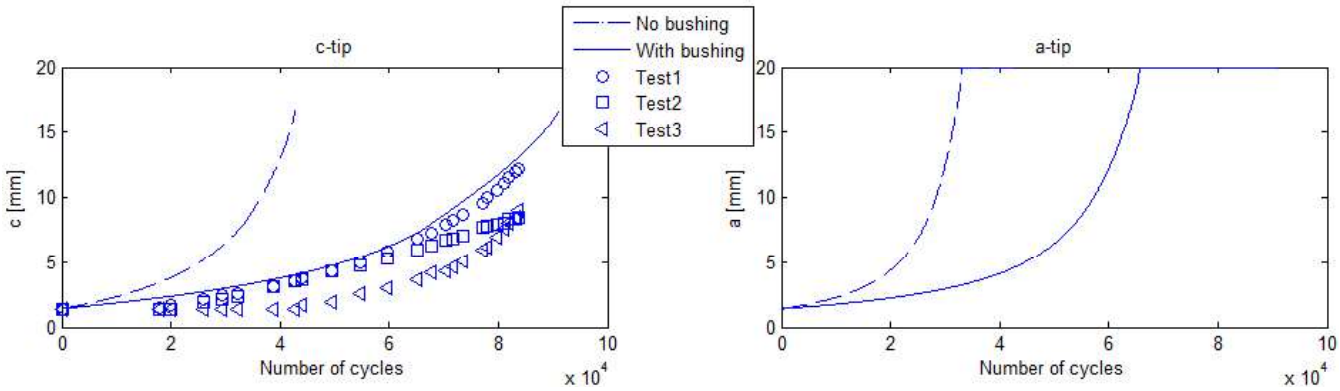

Figure 2.3-2. Comparison tests vs prediction for the axially loaded straight lug.

Tapered lug, spectrum loading

Two tests were performed on spectrum loaded lugs with two corner cracks (crack #1 and crack #2) placed on the opposite sides of the lug hole, see figure 2.3-3. One lug was made of AA7050-T7451 and the other one was made of AA2050-T84. The surface crack lengths were measured continuously. Predictions were based on the following lug data:

Spectrum load applied at 15° inclination
User defined lug, solved by FEM
Lug material: AA7050-T7451 (specimen #1) and AA2050-T84 (specimen #2)
Inner radius = 25.5 mm
Outer radius = 50 mm
Thickness = 24 mm
Bushing inner diameter = 30 mm
Bushing material: Steel
Bushing-lug interference = 0.01 mm

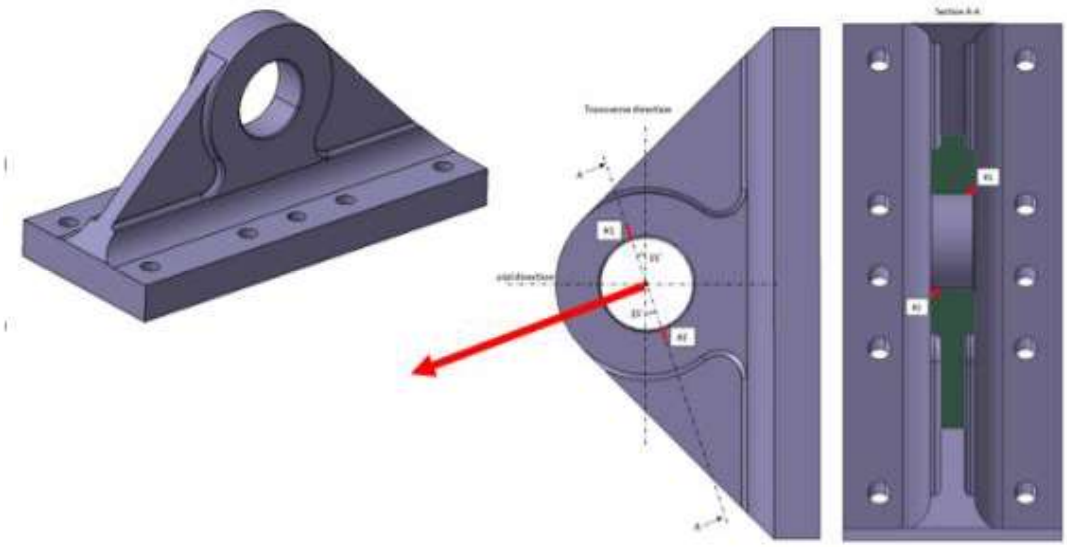

Figure 2.3-3. Specimen geometry.

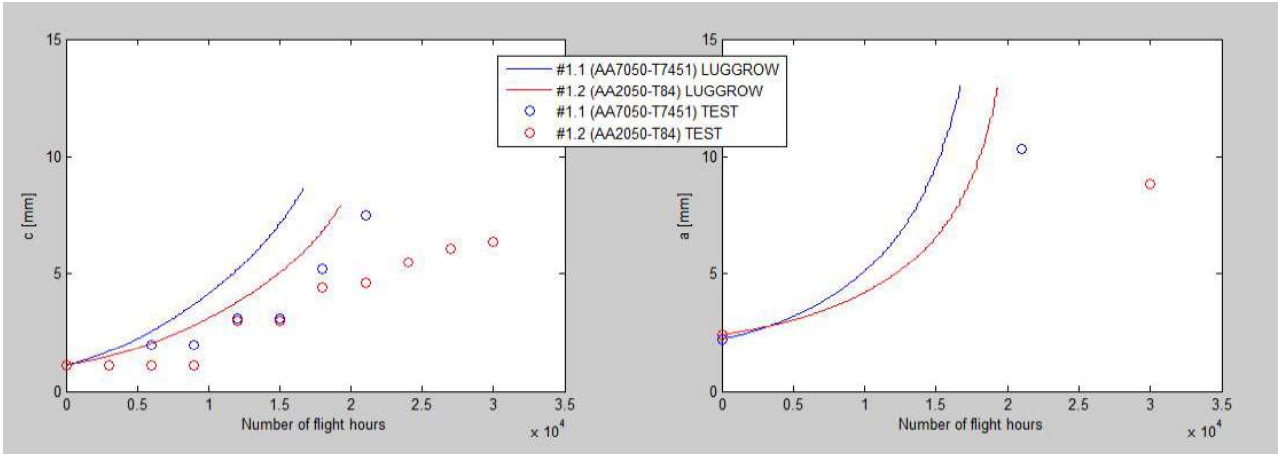

Figure 2.3-4. Crack #1 lengths c and a vs number of flight hours, specimen #1 and #2.

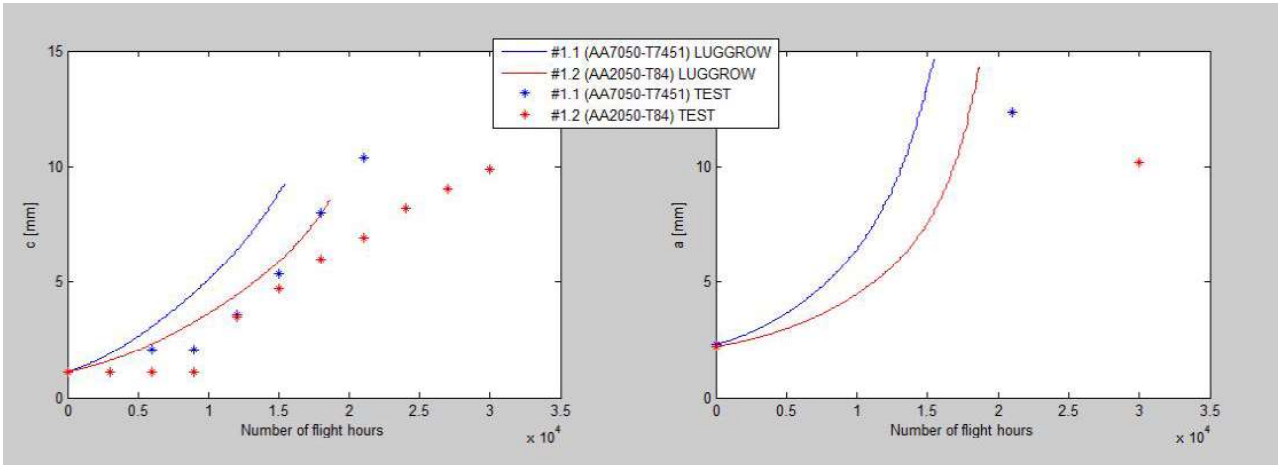

Figure 2.3-5. Crack #2 lengths c and a vs number of flight hours, specimen #1 and #2.

Conclusion

The method for prediction of crack growth in lugs gives slightly conservative results compared to the tests performed. An expansion of the method to include the variation of the load direction is current work in progress.

References

[1] Newman JC. Predicting failure of specimens with either surface cracks or corner cracks at holes. NASA TN D-8244. 1976.

[2] Bowie OL and Freese CE. Elastic analysis for a radial crack in a circular ring. Eng Fract Mech 1972;4:315-321.

2.4 Damage tolerance tests of canard wing pivots made of AA7050-T7451 and AA2050-T84

Hans Ansell, Zlatan Kapidžić, Saab AB

Pivots for Gripen aircraft are made of AA7010-T7451 which is similar to alloy AA7050-T7451 which is the prime choice candidate to replace the no longer available AA7010 alloy. The use of AA7050 instead of the test verified pivot made of AA7010 is not considered to require any additional testing i.e. outcome from the previous test, consisting of canard wing, pivot and actuator arm, can be used to access damage tolerance capability of metal parts through similarity calculations.

An optional change to the less proven and less experienced alloy AA2050 requires renewed testing. The main reason for the need of testing is that the pivot is bi-axially loaded in critical sections. Biaxial stresses give rise to mixed crack modus which is a recognized weak property for aluminium-lithium alloys. A repeated test, in accordance with previous damage tolerance test is considered to be the best approach for certification purposes but a simplified development test in order to challenge AA2050 to be a candidate alloy. The accomplished test was a comparable test where simplified test objects (part of the pivot, no wing) was tested in two embodiments, manufactured in AA2050 and AA7050 respectively.

The aim of the test programme was to show if there were any differences in the damage tolerance capability of a generic canard wing pivot manufactured in aluminium-lithium alloy AA2050-T84 compared to a pivot made of AA7010/7050 alloys.

The test object represented a typical critical sections of the pivot. This means that the test area is limited in size. Due to the nature of the principal loading (bending and torsion) a cantilever test set up was selected. The test object was designed end structure for attachment to a solid wall at one end and to apply loads at the opposite end. The test objects were furnished with a half circular artificial defect, nominal size 2.6 mm deep in the middle of the stress raiser section using electro spark machining.

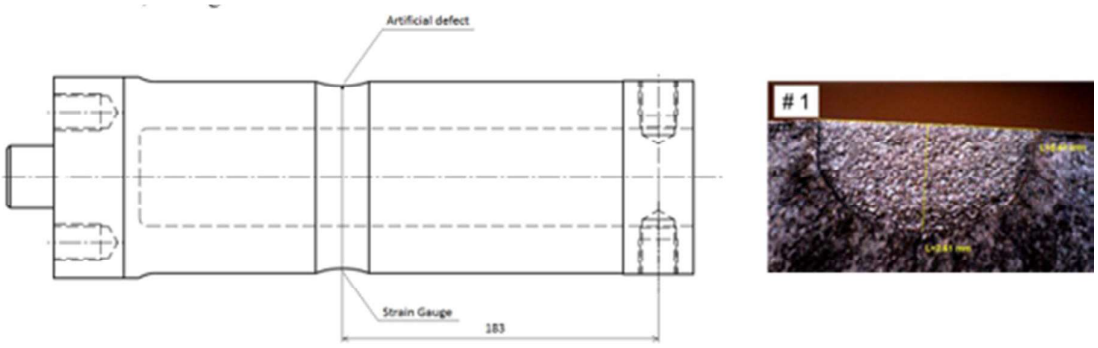

Figure 2.4-1 Test specimen geometry and positions of artificial crack and strain gauge

The test needs two load actuators arranged in a way that prescribed shear and normal stresses occurs in sections of the test area. The shear and normal stresses are governed from application of bending and torsion loads on the test article e.g. in an arrangement with a transverse beam loaded at its ends with load actuators.

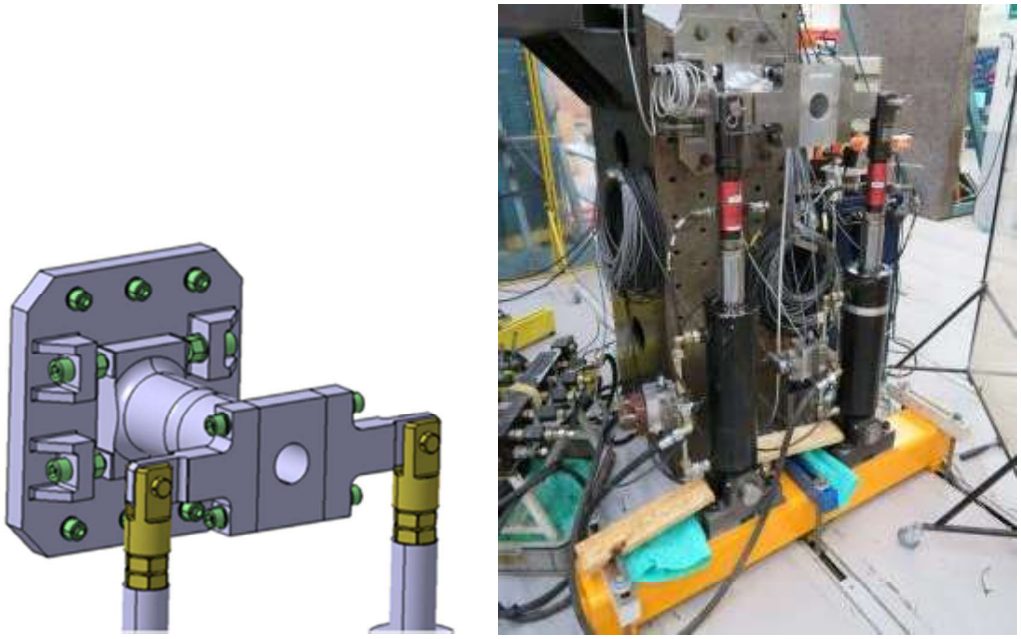

Figure 2.4-2 Test specimen in loading arrangement

A test spectrum was used where insignificant load cycles were eliminated in order to reduce testing time. The elimination was done using the max principal stress in the critical section as the steering stress component. The derived elimination vector was thereafter applied to the individual bending (Mb) and torsion (Mt) moment sequences. The final number of load states in the test sequences was 83,350 which represent 800 h.

Test specimens #1 (AA2050) and #2 (AA7050) were tested under combined bending and torsion with a limit load shear to bending stress ratio of $\tau/\sigma = 0.20$. Test specimens #3 (AA2050) and #4 (AA7050) were tested under pure bending.

The crack in specimen #2 (AA7050) propagated at an angle of about 10 degrees, which coincides with its growth perpendicular to the direction of the max principal stress even though the shallow ditch constituted a certain limitation of deviation. The AA2050 specimen #1 propagated initially in the same way but turned almost 90 degrees at the end of it growth, se figure 2.4-3.

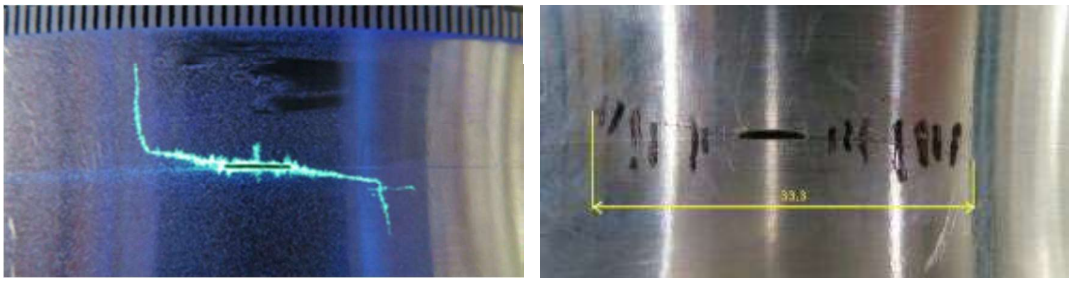

Figure 2.4-3 Crack propagation directions in specimen #1 (AA2050) and #3 (AA7050)

The crack propagation for both torsion/bending and pure bending was recorded and given in the diagram in figure 2.4-4.

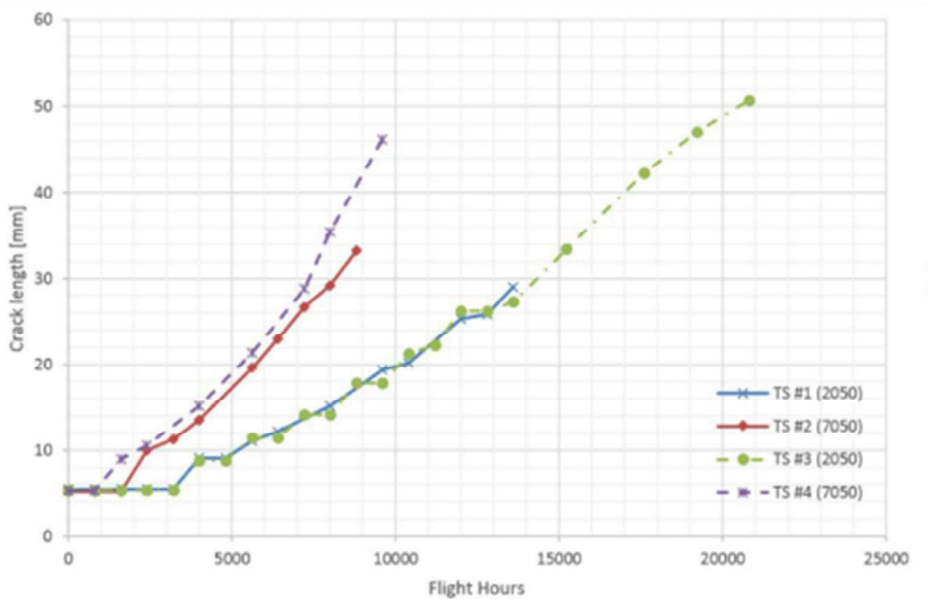

Figure 2.4-4 Crack growth records of all specimens

Specimens #1 and #2 were subjected to a residual strength tests to 125% limit load under combined torsion/bending with no failure. Due to limited actuator capacity failure tests were done under pure bending load. The AA2050 specimen #1 was loaded to the maximum actuator capacity of 220% limit load but did not fail. The AA7050 specimen #2 failed at 217% limit load.

Specimens #3 and #4 (with longer cracks than in specimens #1 and #2) were also subjected to a residual strength test to 125% limit load (pure bending) with no failure. The AA2050 specimen #3 was loaded to the maximum actuator capacity of 220% limit load but did not fail. The AA7050 specimen #4 failed at 160% limit load.

Specimens #1 and #3 made of AA2050 alloy were cut to be able to be pulled apart and showed a significant crack branching behaviour in the fracture surface while specimens #2 and #4 made of AA7050 alloy showed a plane structure, figure 2.4-5.

Figure 2.4-5 Broken specimen #1 (AA2050) and #4 (AA7050)

2.5 Crack growth testing in spectrum loaded notched geometries made of AA7050 and AA2050

Hans Ansell, Zlatan Kapidžić, Saab AB

Crack growth in plates made of Aluminum-Lithium alloy AA2050-T84 has shown different behavior compared to AA7050-T7451, concerning the crack growth rate and the character of the crack surfaces. These results have been obtained by testing of generic specimens, designed for derivation of dimensioning data, which do not contain stress concentrations which are commonly present in aircraft structure. The aim of this testing series is to evaluate the crack growth rate and the crack growth characteristics for the two mentioned materials, using specimens which include structure like stress concentrations. The results shall also be used to evaluate the predictions produced by the crack growth models used for damage tolerance dimensioning.

Specimens
The test series include spectrum and residual strength testing of three types of pre-cracked specimens:

- Plate with radius, surface crack in radius, type (R), 12 specimens
- Plate with hole, corner crack in hole, type (H) , 10 specimens
- Plate with pin-loaded hole, corner crack in hole, type (P) , 11 specimens

see, figures below.

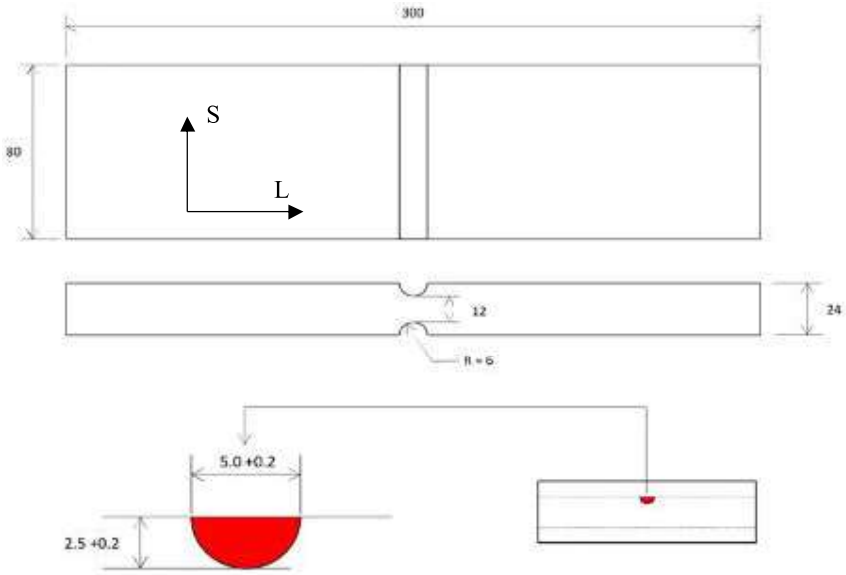

Figure 2.5-1. R-type specimen with a surface crack.

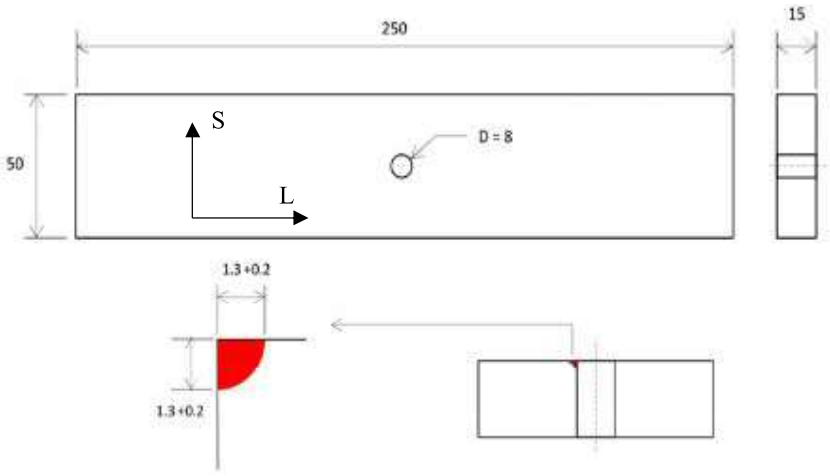

Figure 2.5-2. H-type specimen with a corner crack.

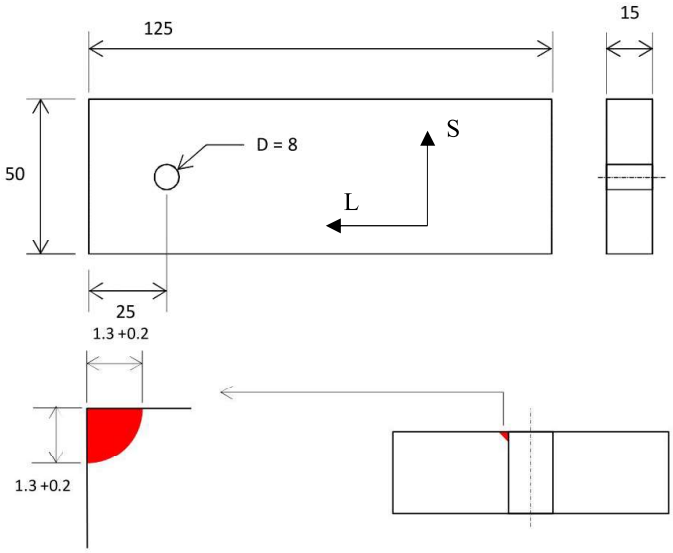

Figure 2.5-3. P-type specimen with a corner crack.

Each individual specimen is given a name written according to a designation code:

Specimen type Material: Specimen number
For instance R2:1 means, R-type specimen made of 2050, number 1.

Load Spectra
Two different load spectra were used in this testing series, UVKB and BFKB.

Wing spectrum UVKB:	Asymmetric, tensile dominant load spectrum, which represents the load variation in the lower wing attachment.
Fin spectrum BFKB:	Symmetric load spectrum which represents the load variation in the fin attachment.

Test arrangement and measurements
The testing is performed in a servo-hydraulic testing machine. Specimen types R and H are simply clamed at both ends in the loading frames of the machine. Specimen type P is clamped at one end while the hole is loaded on the other end by a steel pin, which is connected to the loading frame via a loading fork.

Crack measurements were performed in order to establish the relation between the crack length and the number of flight hours passed. For specimen type R, both crack tips are visible and are measured. In specimen types H and P, only the surface crack tip is measured. The cracks are frequently photographed during the cycling and measurement of the crack length is performed a posteriori in the photographs.

Crack growth calculations
Crack growth calculations in AFGROW [1] have been performed for the purpose of comparison with the test results. AFGROW appropriate classic stress intensity factors have been used.

Results
The main test results that are compared between the materials and to the calculations are crack length as function of number of flight hours and the residual strength. The comparisons are performed below for R and H specimen types and photographs of some of the broken specimens are shown. P-type specimen tests are still to be performed.

Crack growth test and calculation results

R-type specimens

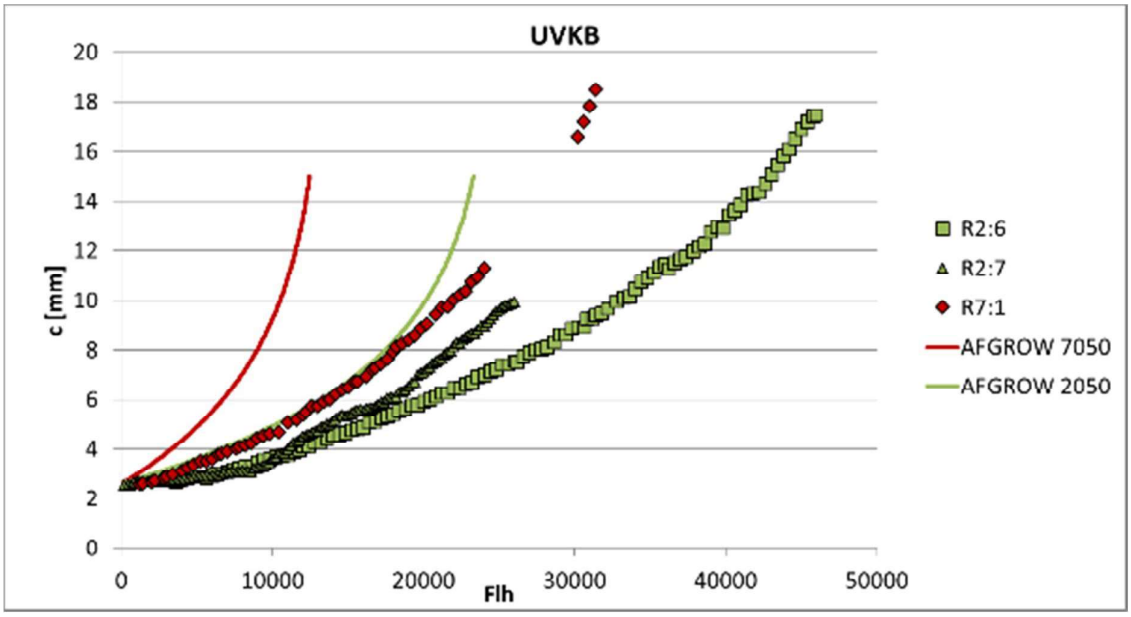

Figure 2.5-4. Surface crack length, UVKB spectrum, R-type specimen, test vs prediction.

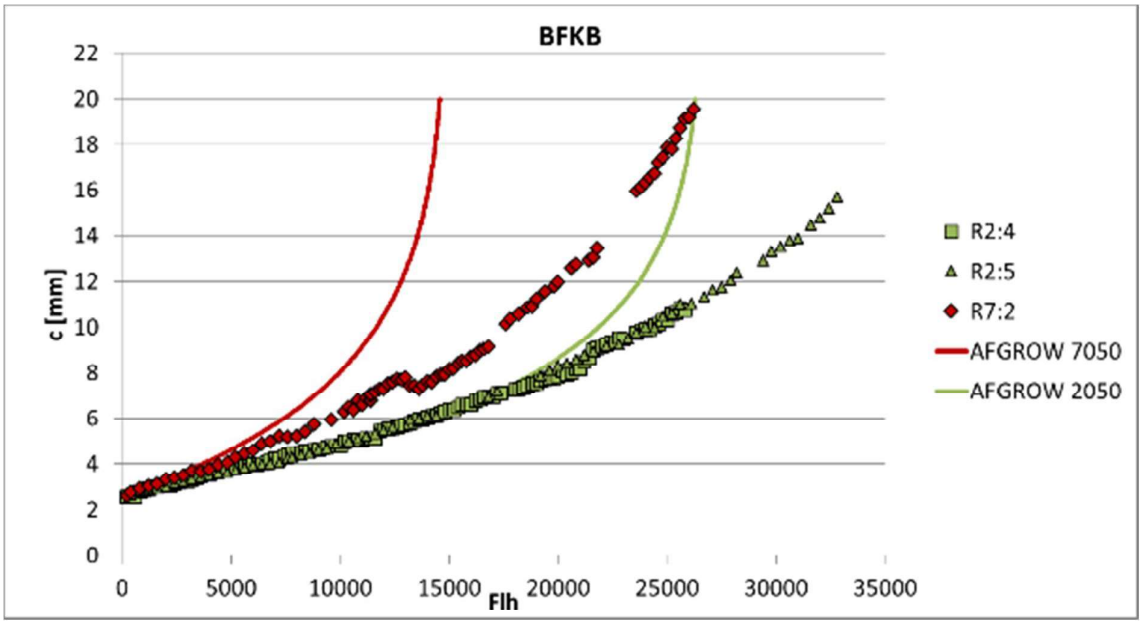

Figure 2.5-5. Surface crack length, BFKB spectrum, R-type specimen, test vs prediction.

Figure 2.5-6. R7:1, 7050, UVKB.

Figure 2.5-7. R2:2, 2050, UVKB.

Comments regarding R-type specimens:

- Stable slow crack growth was achieved in all specimens and the cracks grew through the thickness of the specimens as shown in Fig 2.5-6 and 2.5-7.

- In 2050 specimens the cracks grew 1.3-1.5 times slower than in 7050 specimens.

- The predictions with AFGROW were generally conservative compared to test results. One of the possible reasons is probably the lack of consideration of load sequence effects. The predicted crack growth was approximately 2 times slower in 2050 than in 7050 specimens.

- The crack surface is somewhat rougher in 2050 specimens than in 7050 specimens, especially at large crack length.

H-type specimens

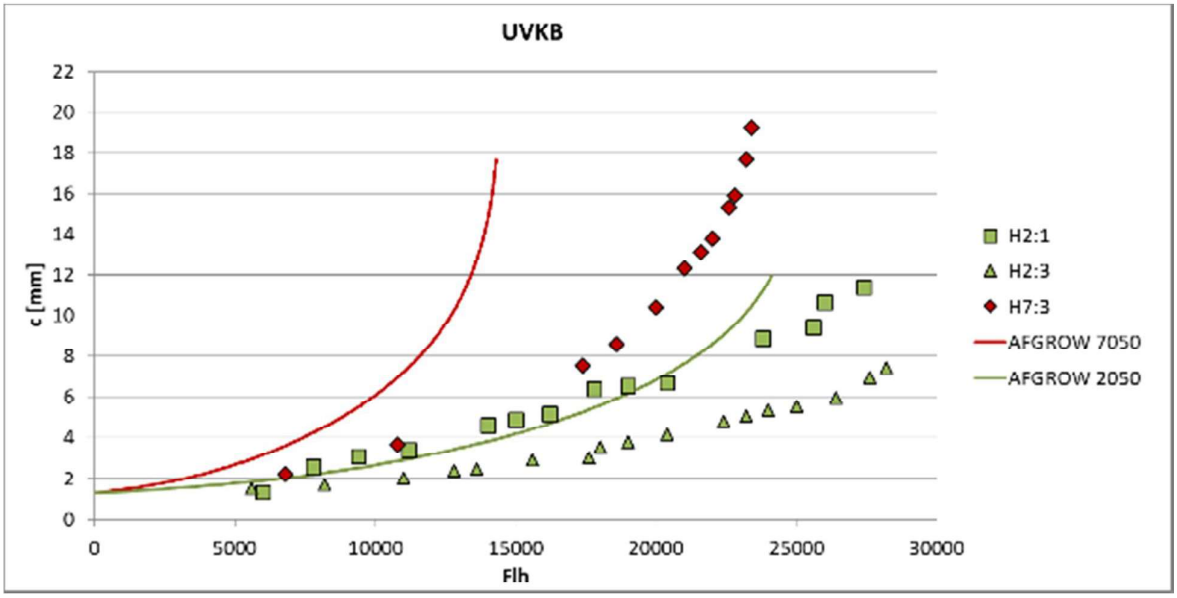

Figure 2.5-8. Surface crack length, UVKB spectrum, H-type specimen, test vs prediction.

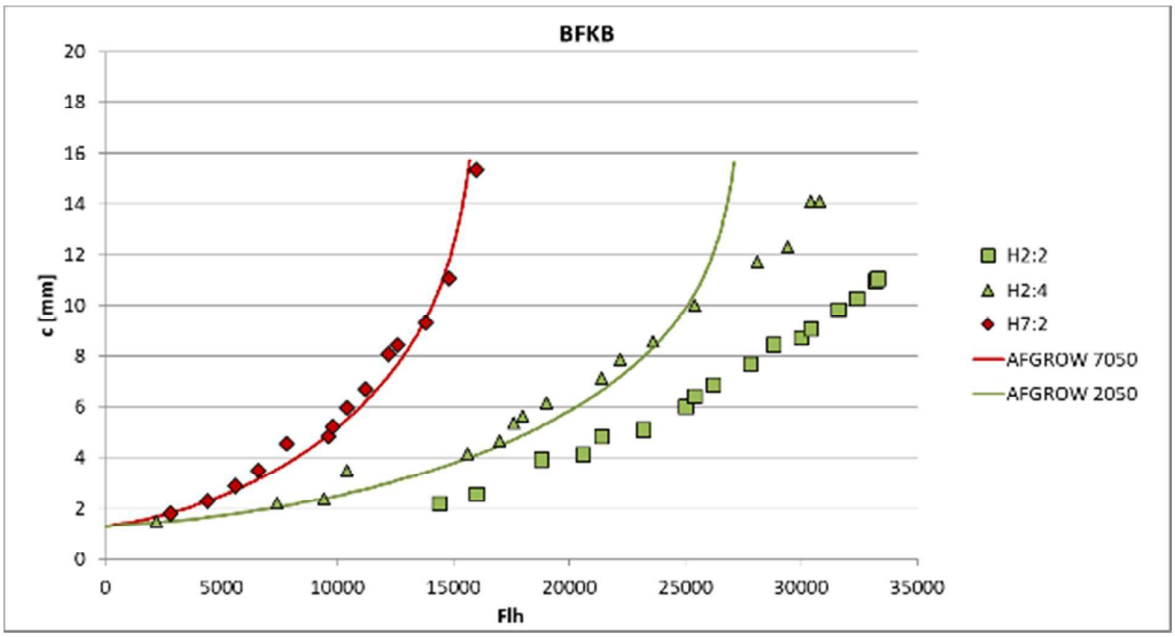

Figure 2.5-9. Surface crack length, BFKB spectrum, H-type specimen, test vs prediction.

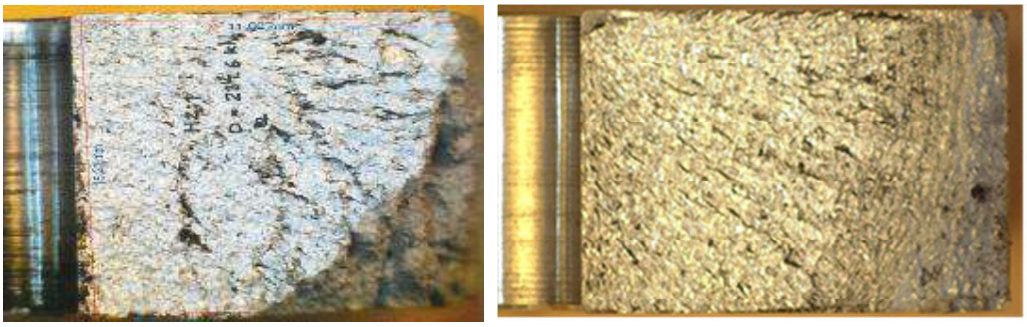

Figure 2.5-10. H2:1, 2050, UVKB (left), H7:2, 7050, BFKB (right)

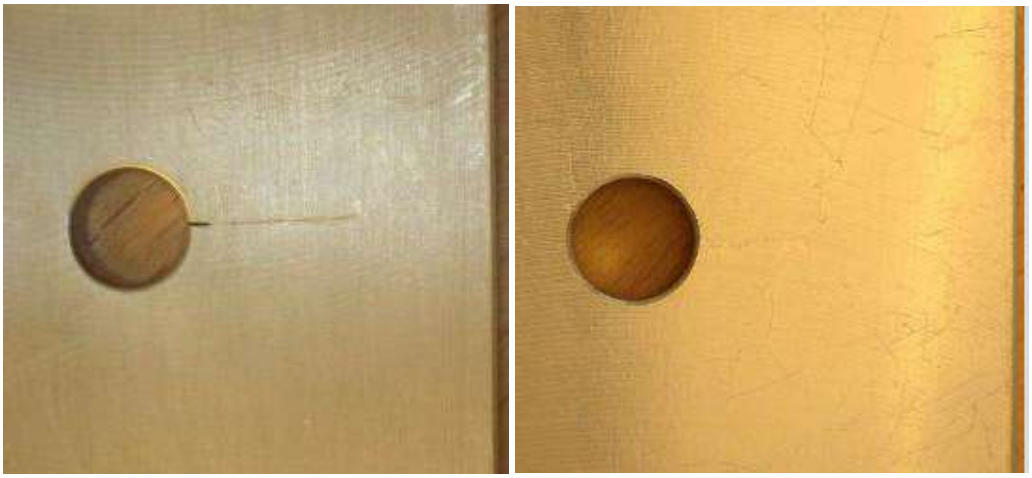

Figure 2.5-11. H2:2, 2050, BFKB, upper side (left) and lower side (right).

<u>Comments regarding H-type specimens:</u>

- Stable slow crack growth was achieved in all specimens and the cracks grew through the thickness of the specimens as shown in Figs 10-11.
- In 2050 specimens the cracks grew 1.3-1.9 times slower than in 7050 specimens.
- The predictions with AFGROW were generally conservative compared to test results for UVKB spectrum and coincided with the tests for BFKB spectrum.

Conclusions

- In all compared cases, the cracks grew slower in AA2050-T84 than in AA7050-T7451. The crack growth rate depends on the specimen type, the spectrum and the crack length, but can be roughly estimated to be 1.3-1.9 times slower in AA2050-T84 than in AA7050-T7451.
- None of the predictions of the crack growth were un-conservative compared to the test outcome.
- P-type specimen tests are still to be perfomed.

References

[1] AFGROW. User's guide and technical manual. Version 5.02.05.18. February 2014.

2.6 Development of fatigue data for longitudinally loaded lugs in Aluminium-Lithium alloy AA2050-T83 and adaption to fatigue design method.

Hans Ansell, Saab AB
Enna Arasto, VTT

This chapter highlights the international cooperation research activities in between Saab Aeronautics (Sweden) and VTT (Finland).

Saab Aeronautics applies an in-house developed calculation method and sizing procedure for the fatigue strength of lug joints, [1]. The method has been used in all aircraft projects since the late 60s together with related fatigue materials data for a number of aluminium alloys and steels. The method handles lugs of basic design and lugs furnished with bushings with or without interference fit. Special parameters account for oblique loaded lugs and specifies allowed cumulative damage sums for the application to variable amplitude loading. Scatter reduction factors are specified to meet design practice regarding safe-life design.

Fatigue tests have been made by VTT of longitudinally loaded lug of Aluminium-Lithium alloy AA2050-T84 since the alloy can be a candidate to replace lug joints currently made of alloy AA7050/7010-T7451. The test programme was intended to produce fatigue data necessary for the application of the lug design method to lug made of alloy AA2050-T84. A total of 44 longitudinal loaded lug specimens were specified for the purpose with some additional specimens kept in spare. A total number of 51 specimens were finally tested. Two lug geometries were defined, A and B, and the B lug configuration consists of variants with and without bushings, net fit and interference fit. Two orientation of specimens regarding product form directions were included, longitudinal (L) and short transverse (ST). The main number of the specimens were tested under constant amplitude loading and a smaller number under variable amplitude loading for checking purposes. The dimensions of the specimens, pins and bushings are given in Figure 2.6-1.

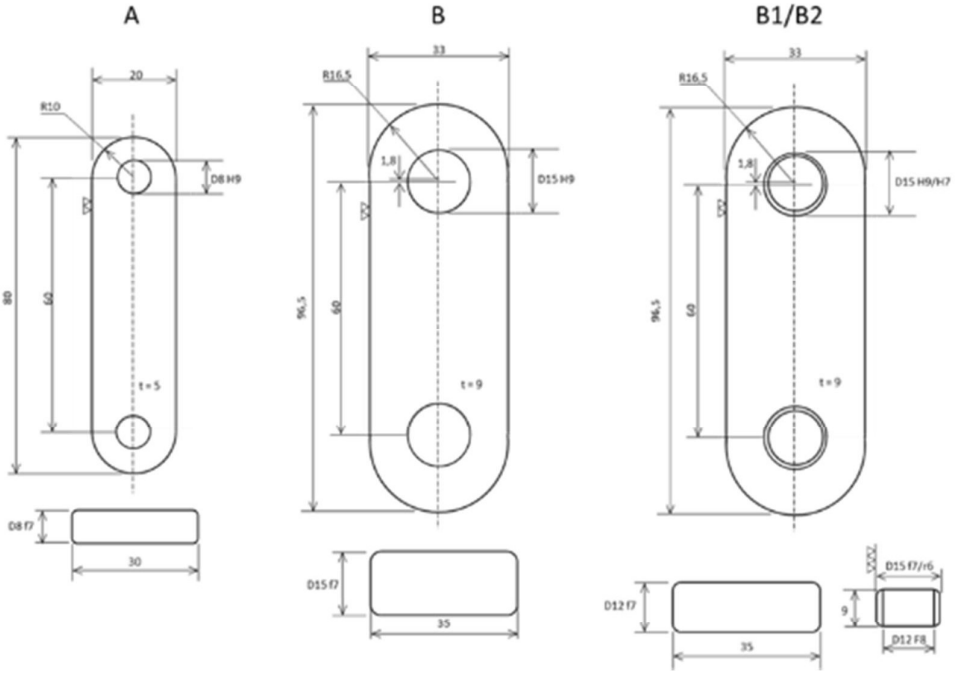

Figure 2.6-1 Lug specimens.

All constant amplitude testing were be done at a cyclic minimum stress of 10 MPa. The maximum stress levels were selected in order to obtain relevant SN-curves.

In Figure 2.6-2 are some results for lugs of type A (net fit, no bushing) loaded in the longitudinal (L) direction shown together with some previously obtained results for the same type of lugs made in AA7010-T7451. There is a tendency to lower fatigue strength in the high cycle regime for these simple net fit specimens without bushings.

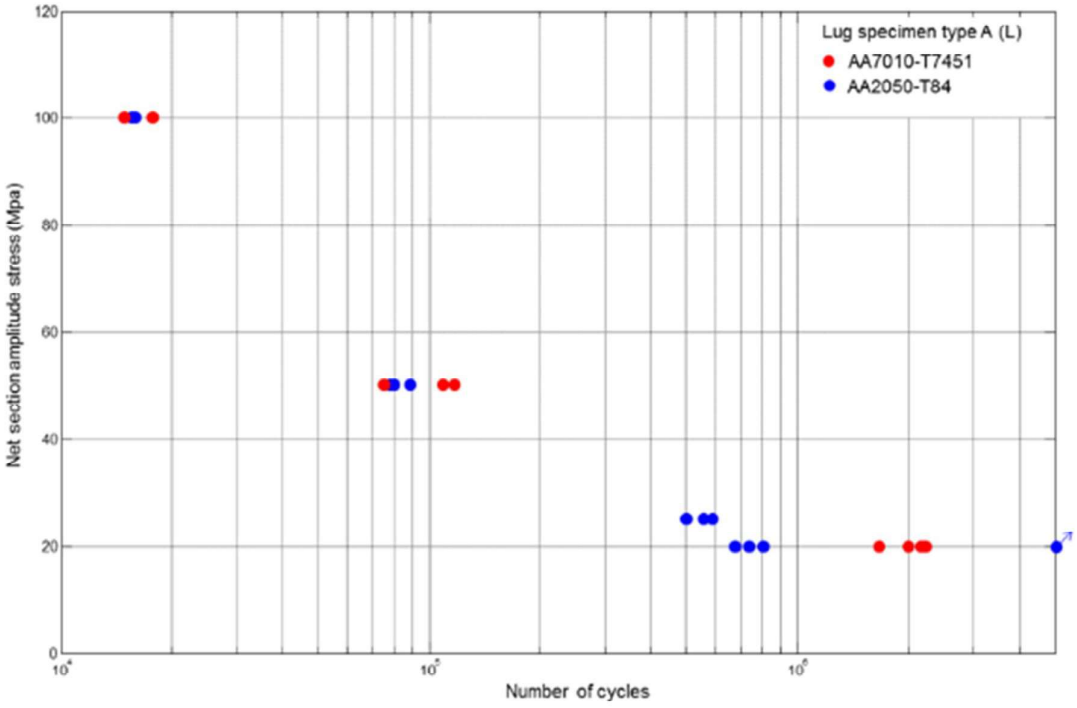

Figure 2.6-2 SN test data for type A lug specimens made of AA7010-T7451 and AA2050-T84.

The variable amplitude testing was done with the type B2 lug configuration installed with a lubricated bushing with interference fit. The loading was based on a fighter wing bending type spectrum. The spectrum has been used for many general materials investigations within Saab Aeronautics, also in the previous lug tests for AA7010-T7451 with a mean life of 30 000 flight hours. The load sequence were truncated from compression load states for use in the longitudinal lug testing. The target mean life was set to 30 000 flight hours for the L-oriented lugs and a peak spectrum stress level of 200 MPa. The actual obtained mean life was 32 000 flight hours for the L-oriented lugs and 13 000 flight hours for the ST-oriented lugs i.e. about a factor of 2.5 shorter life in the ST-direction.

The experimental data are converted to a “reference” lug geometry according to [47].
The influence of bushing and fit are accounted for by application of a cycle dependant adjustment factor ų. This fitted factor together with the experimental SN-curves for lug of basic geometry are used to derive SN-curves for lugs with special conditions, e.g. bushing, lubrication, interference fit. The SN-curves together with other parameter settings are used to construct complete Haigh-diagram

2.7 Static strength sizing of metal components with FE methods

Rikard Rentmeester, Zlatan Kapidžić, Saab AB

The goal for this project is to develop recommendations for in-house FEA for ultimate strength of details for which available handbook methods are unavailable or too conservative. The recommendations will include specific material data as well as recommendations for the set-up and post processing of non-linear finite element analyses.

Traditionally, machined details of metals are dimensioned by means of handbook methods or similar. The increasing demands on the performance to weight ratio results in a need to decrease the conservatism in strength analysis in order to reduce weight. The finite element method (FEM) can be used for many analysis in order to obtain a more accurate result compared to handbook solutions, which sometimes are too conservative. Such finite element analysis (FEA) generally include geometrical as well as material nonlinearities.

The material description required for non-linear finite element analyses is more extensive than what is generally given in the currently available data. Currently, the data is limited to the yield and the ultimate strength in tension for many metallic material, whereas the full stress-strain curve is needed in a finite element analysis.

Furthermore, the failure limit must be defined. In sections where the strain distribution is homogeneous, the use of ultimate tensile strength may be fair, whereas this criterion can be way too conservative if redistribution of load path during plastic takes place. In such cases the strain distribution can vary significantly across the cross section. Such variation may occur in cross sections with notches or cross section which are subjected to a load that results in an inhomogeneous stress and strain distribution. If the structure is considered to fail as soon as one single material point has reached the plastic strain corresponding to the ultimate tensile strength, the predicted ultimate load will be conservative for ductile materials.

The workflow for this project are the following:

1. Conventional uniaxial tensile tests are performed on a strategic choice of materials, which are commonly used at SAAB. This is done to obtain the full stress-plastic strain curve. The goal is also to obtain a plausible but yet conservative failure strain from these tests. Five materials are included in the investigation; 7050 aluminium, 2050 aluminium-lithium, Ti-6Al-4V titanium allow, 4330 M steel alloy and 15-5 PH steel.

2. Two artificial structural tests are made on coupon level. The first test is a small compact tension (CT) specimen with a number of open holes, see Figure (a). This geometry has been used before as a Round Robin test in Ref. [1].
   The second test is a four point bending of a beam with two open holes, see Figure (b). This test will result in a redistribution of load path during deformation. It is possible that the force carried by the beam continues to increase also after a local failure due to load path distribution.

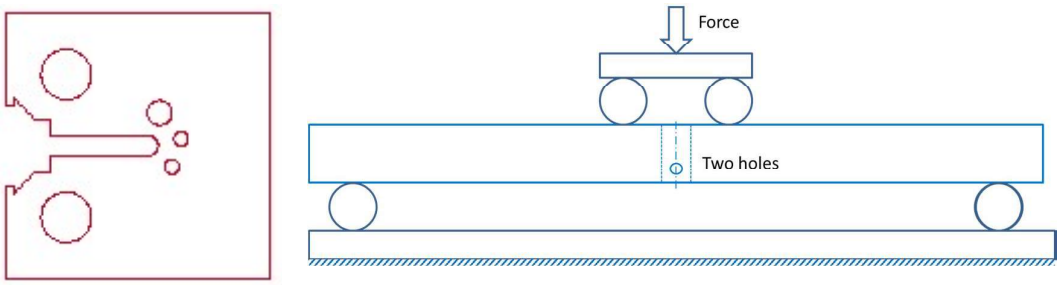

(a) (b)

Figure 2.7-1 (a) Compact tension specimen with open holes and (b) 4 point beam bending test set up.

3. Perform state of the art FEA of the component tests in order to validate methodology. An example of a FEA is shown in Figure 2.7-1. These analyses may include both material data and failure criteria which is inoperable in practise in the product development process.

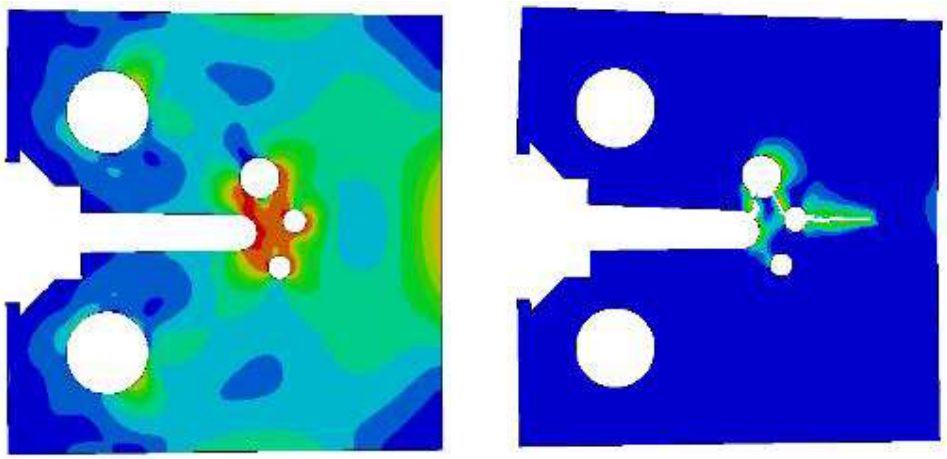

(a) (b)

Figure 2.7-1. Example of results from a FEA of the CT specimen with open holes. The effective stress before failure (a) and a snapshot of the distribution of effective plastic strain during progressive failure (b).

4. Redo the FEA of the component tests with the same data which is currently available for all materials. This generally does not include the full stress-strain curve, especially not for strains beyond the onset of diffuse necking.

5. Formulate a methodology to be used in FEA originating from the currently available data.

A great part of the methodology consists of good material data. The data found in this project does not cover the entirely group of materials that are used at SAAB, and for materials excluded in this project, there is a lack of data. The goal is to construct an approximate, yet good enough, stress-strain curve from available data.

[1] Boyce B.L., et al. (2014) The Sandia Fracture Challenge: blind round robin predictions of ductile tearing Int. J. Fract. 186 pp. 5–68

2.8 Creation and Verification of World's largest K_I-Databases for Twin Cracks at a Hole in a Plate

Börje Andersson, BARE

The objective of the project was to develop complete, and final, databases with stress intensity functions $K_I(\phi)$, for twin cracks at a hole, straight shank or countersunk, in a large plate subject to tension, bending and pin-loading, see Figure 2.8-1. The derived K_I-data are virtually exact, *i.e*. the relative *error* in K_I at an arbitrary point $\phi = \phi^*, 0 < \phi^* < \bar{\phi}(a,c,b,t,R)$ on the crack front is less than 10^{-3}, for all 180 million $K_I(\phi)$– graphs derived, which we guarantee by using state of the art mathematical-numerical schemes and advanced verification procedures.

Joint Type Analysed	Parameter Values				Total Number of Scenario
	c/a	a/t	R/t	b/t	
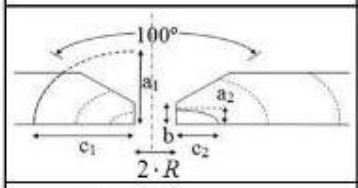	25	25	30	4	21.92 *M*
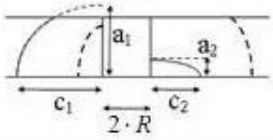	25	23	30	1	4.32 *M*
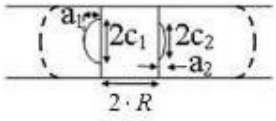	25	23	30	1	4.32 *M*

Figure 2.8-1. Geometries analysed which provided over 180*M* high-accuracy $K_I(\phi)$-graphs for tension, bending and wedge-loading for $\approx$30*M* unique twin crack scenario.

Points in the $(a_i/t, c_i/t, b/t, R/t) - K_I(\phi)$ spaces were selected sufficiently close in order to avoid significant interpolation errors in a fatigue analysis. Table 1 shows the parameter set analysed. Calculated data are valid for Poisson's ratio 0.3.

Parameter	Values
c/a	0.1, 0.111, 0.125, 0.1428, 0.1667, 0.2, 0.25, 0.333, 0.5, 0.667, 0.75, 0.8, 1.0, 1.25, 1.333, 1.50, 2.0, 3.0, 4.0, 5.0, 6.0, 7.0, 8.0, 9.0, 10.0
a/t	0.1, 0.2, 0.3, 0.4, 0.5, 0.6, 0.7, 0.8, 0.9, 0.95, 0.975, 0.99, 1.05, 1.15, 1.50, 1.75, 2.0, 2.5, 3.0, 4.0, 5.0, 6.0, 7.0, 8.0, 9.0, 10.0
R/t	0.075, 0.1, 0.111, 0.125, 0.1428, 0.1667, 0.2, 0.25, 0.333, 0.4, 0.4444, 0.5, 0.5714, 0.667, 0.75, 0.8, 1.0, 1.25, 1.333, 1.50, 1.75, 2.0, 3.0, 4.0, 5.0, 6.0, 7.0, 8.0, 9.0, 10.0
b/t	0.05, 0.25, 0.50, 0.75, 1.0

Table 1. Database parameter space.

A difficulty in storing and using data for fatigue crack growth analysis is that about 50% of the 180*M* $K_I(\phi)$-graphs have maximum values which theoretically are *infinite* at one crack front vertex, i.e. vertices v_5 and v_6 in Figure 2.8-2. In the paper [1] we advise a technique to quantify the near-vertex behaviour virtually exactly with one single number, the so-called Vertex intensity factor S_I, which we compute for all scenarios that have a crack with infinite stress intensity factor values at a vertex.

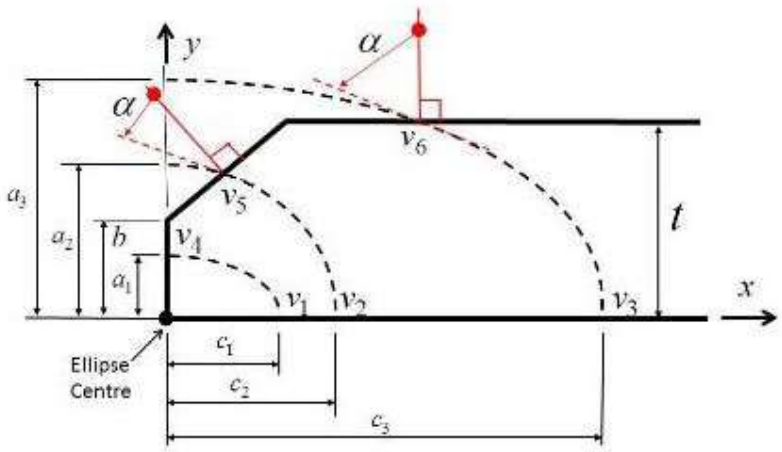

Figure 2.8-2. Three characteristic crack geometries at a countersunk hole geometry.

The value of the stress intensity function close to such a vertex is determined from equation (1).

$$K_I(s) = S_I \cdot s^{\Lambda(\alpha)-1/2} \qquad (1)$$

Where *s* is the distance to the vertex and $\Lambda(\alpha) < 1/2$ is given in [1].

The numerical methods used in the work rest on an over 30 years' long development of the FE-software STRIPE which is based on an *hp*-version of FEM which, when proper FE-meshes are used, as in the present work, provide exponentially fast convergence to the exact 3D mathematical solution. Advanced post-processing procedures are used to extract stress intensity functions $K_I(\phi)$, where again, all point-wise K_I-values converge exponentially fast to the exact mathematical values for the 3D problem. A mathematical *splitting* method, based on a solid mathematical foundation is used to decrease the computational costs by a factor of over one thousand without sacrificing solution accuracy (i.e. keeping the point wise error $< 10^{-3}$ at arbitrary points at all *180* million crack fronts). New methods developed in the present project consist of reducing round-off errors when analysing large and very thin plates, developing the mathematical splitting method to apply to countersunk crack geometries, developing a procedure for verification of computed point-wise K_I-data and implementing the methods on massively parallel computer systems with thousands of compute nodes, each with 24-32 cores. The FE-meshes needed are created using five newly developed mesh generators which create the 50*k* single crack meshes used which are optimized for the *hp*-version of FEM.

It is believed that the data bases generated in the present work closes a 40 year old search for reliable $K_I(\phi)$-data for the three important crack geometries shown in Figure 2.8-1. Currently, the intent is that these large data bases, containing together over 180*M* high-accuracy *verified* K_I-solutions will be delivered to the fatigue community via the AFGROW-, and possibly, the NASGRO-fatigue analysis software.

Referens

[1] Börje Andersson and James Greer, Jr., “Creation and Verification of World’s largest K_I -Databases for Multiple Cracks at a Countersunk and Straight-Shank Hole in a Plate subject to Tension, Bending and Pin-Loading”, Proceeding of 29 th ICAF Symposium, Nagyoa, 7-9 June, 2017, 10 pp.

2.9 Structural integrity of repaired monolithic metal structure

Hans Ansell, Saab AB
Anders Klarbring, Ulf Edlund, Bo Torstenfelt, Linköping University

Primary load carrying structures in fuselages are mainly manufactured from machined and/or forged single pieced parts. Such parts are weight optimized and contain most often stress raisers of various kinds e.g. cut-outs, thickness steps, interacting radii which make them prone to fatigue failure. The number of such hot-spots seems to increase when designing with digital modelling techniques thus pushing the failure probability to rise and strain the risk budget. If fatigue cracking occurs during service life it is costly and impractical or most often impossible to replace these parts. A repair procedure to restore flight safety and availability is needed which includes several challenging engineering activities which involve research work.

Inventory and problem definition

An inventory is made of typical aircraft primary structural components prone to fatigue cracking. Typical structural design parameters are identified such as pocket sizes, thicknesses, holes and cut-outs and related significant design load cases. Based on these findings, generic damages scenarios are defined as starting points for further analysis and demonstration.

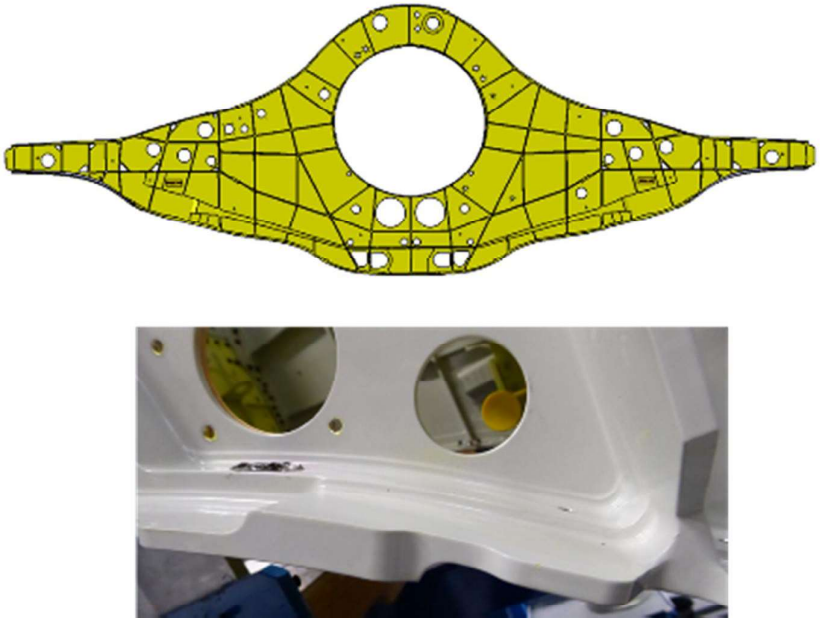

Figure 2.9-1 Monolitic structures

Model Formulation and mechanical experiments

The topology optimization problem is defined by relevant objective functions and constraints. Both stiffness constrains and stress intensity factor constrains are evaluated. Theory defined in [1]. The problem of simulation of bonding together with the topology optimization shall be able to handle. A number of crack/patch scenarios are studied and fatigue testing are conducted to support the modeling work and to show that the model concept is relevant.

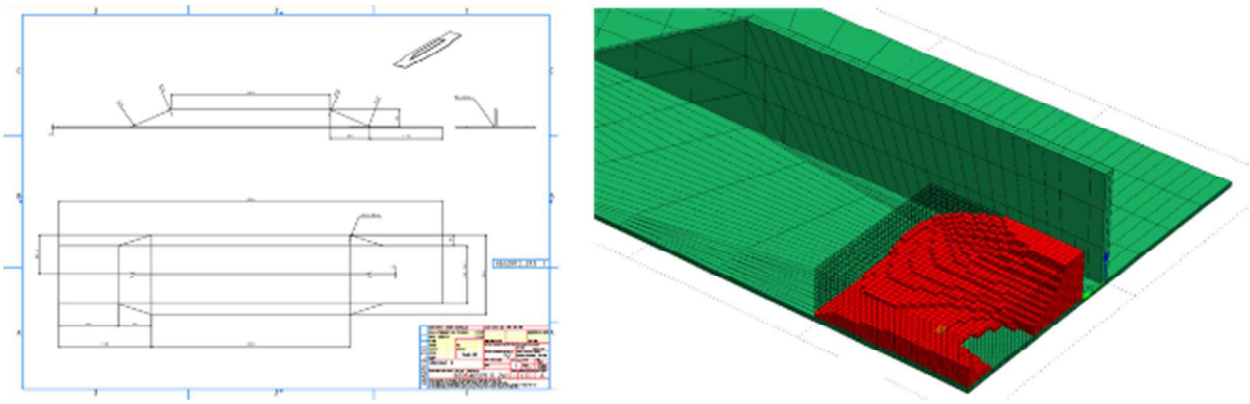

Figure 2.9-2 Test specimen and topology optimized patch

Implementation of the FE systems and scale-up for general applications.

The models developed are implemented in FE software Trinitas for general application and demonstration of the applicability of general repairs. A full-scale demonstrator will be manufactured in which repair patches are included.

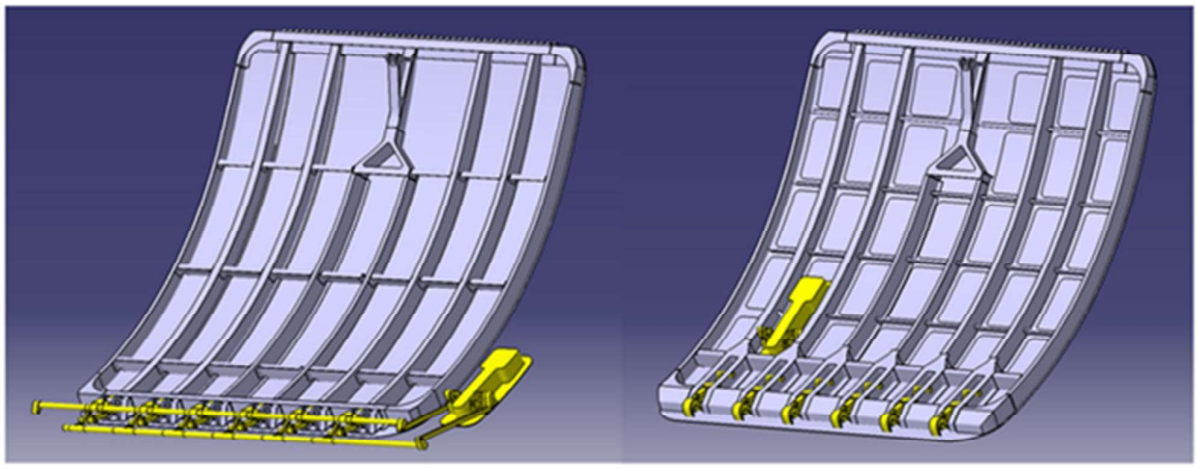

Figure 2.9-3 Monolitic door to be used for application of optimized patches

2.10 Fatigue Behaviour of Additive, Manufactured Ti6Al4V in Aerospace Applications

Magnus Kahlin, Hans Ansell, Saab AB
Johan Moverare, Linköping University

Background

Additive Manufacturing (AM) is a group of manufacturing methods that allows the manufacturer to produce parts with complex geometries that would be difficult or impossible to produce using conventional production methods. AM is considered to have great potential to be used in aerospace structures, contributing to improved part performance, for example light weight designs, and thereby reducing fuel consumption, increase flight range and payload. There are, however, some challenges to solve before AM can be fully introduced in critical aerospace applications. One challenge is the poor fatigue strength of AM parts with as-built surface. The surface of as-built AM parts is very rough and partially melted powder grains creates micro notches which act as stress concentrations. Moreover, the design freedom of AM can create new design features that add additional stress concentrations to the part, see figure 2.10-1

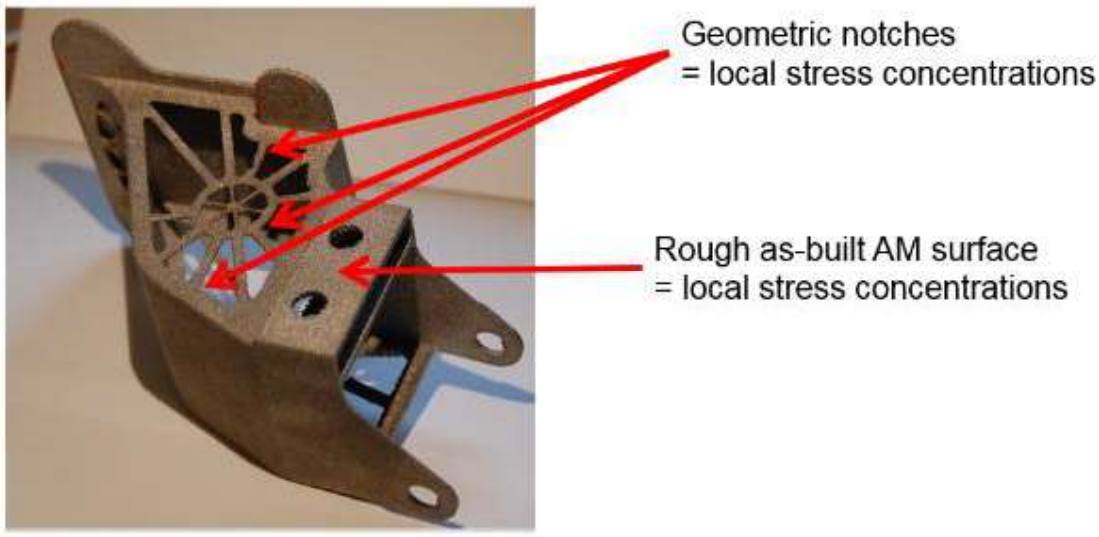

Figure 2.10-1. Aerospace part (demonstrator) re-designed for AM in order to reduce weight.

Fatigue Investigations

The fatigue properties of Ti6Al4V material produced with both Electron Beam Melting (EBM) and Laser Sintering (LS) have been investigated with focus on the effect of the rough as-built AM surfaces. In addition to this, a combined fatigue effect of a geometric notch, built by AM and the rough as-built surface in the notch have been studied as illustrated in figure 2.10-2 [1].

The fatigue notch factor, K_f, have been determined for both machined and rough as-built surfaces for material with and without Hot Isostatic Pressing (HIP) treatment.

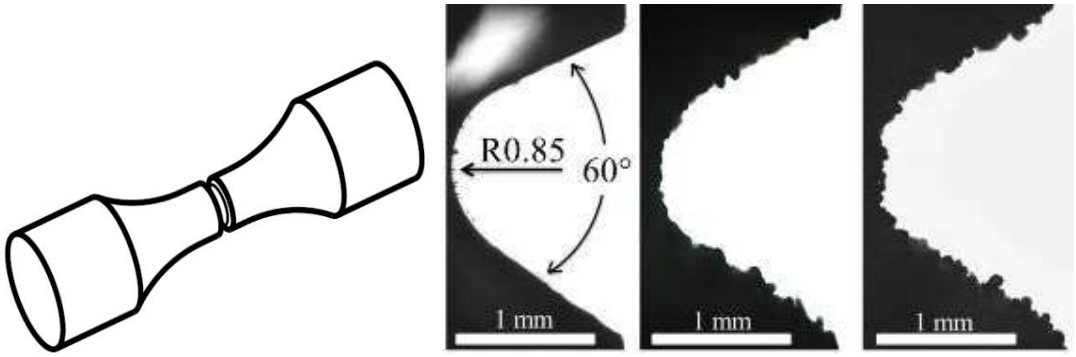

Figure 2.10-2. Notched fatigue specimen (left). From left to right; machined notched, LS as-built notch and EBM as-built notch [1].

Conclusions

The fatigue properties of AM material with as-built roughness are dominated by the roughness of the surface rather than by internal defects and Hot Isostatic Pressing (HIP) has therefore negligible effect on the fatigue properties [1].

The rough as-built surface gives rise to stress concentrations which correspond to a fatigue notch factor, K_f, of 2.8 for Laser Sintered (LS) Ti6Al4V and 4.3 for Electron Beam Melted (EBM) Ti6Al4V [1]. The rough as-built AM surface combined with a AM built geometric notch increased the local stress concentration and reduced the fatigue strength even further which correspond to a K_f= 6.1 for LS and 6.6 for EBM material which is a major fatigue strength reduction [1].

Further work to improve the surface roughness of AM parts need to be performed in order to increase potential applications for AM in structural loaded aerospace parts.

Reference

[1] Kahlin M, Ansell H, Moverare JJ. Fatigue behaviour of notched additive manufactured Ti6Al4V with as-built surfaces. Accepted by International Journal of Fatigue, 2017.

3 FATIGUE AND DAMAGE TOLERANCE CHARACTERISTICS OF COMPOSITE MATERIAL AND STRUCTURE

3.1 Static testing and failure simulation of shear loaded composite-aluminium bolted lap joints

Zlatan Kapidžić, Saab AB

Quasi-static testing of shear loaded composite-aluminium bolted joints, with varying width, fastener type, fastener pretension and bolt hole reinforcement was performed. Simulations of the failure were done using FE and including material failure models for the composite and the metal. The results are to be used as a verification for detailed failure modelling technique.

In design of bolted joints against failure, several parameters need to be taken into account: load type, fastener type, load transfer, pretension, clearance, environmental conditions, failure modes etc. Joints including fibre composite laminates are designed for static loads using the method described in [1]. Essentially, a two-dimensional stress state around a fastener hole is assumed and solved using the complex variable approach. Thereafter a simple failure criterion is applied to estimate the failure load and the mode of failure. The different parameters affecting the joint are considered by applying factors on the solution. This design method, although being robust and straight-forward, has drawbacks regarding the conservatism built in to the failure criteria and in the way the knock-down factors are determined. A more refined way of modelling the failure is by three-dimensional, detailed finite element technique, as in [2], where the different joint parameters affecting the failure can be accurately represented. Results from such modelling can then be used to verify and improve the design method.

In order to validate the predictive capability of the finite element based composite failure model in [2], quasi-static experimental testing of composite-aluminium bolted joint specimens was performed. The parameters considered in the testing programme were:

- Fastener type (protruding head or countersunk)
- Failure mode (net-section and/or bearing failure)
- Secondary bending
- Pretension
- Hole reinforcement (LOCOMACHS [3])

FE-simulations including the composite failure model from [2] and plastic failure of the metallic parts were performed using Abaqus.

Test specimens

Three types of CFRP-aluminium specimens, were tested in order to study the effects of the fastener type and the secondary bending: double-shear specimens with protruding bolt heads (DS-P), single-shear specimens with protruding bolt heads (SS-P) and single-shear specimens with countersunk bolt heads (SS-C). All specimens were fastened by two 6 mm titanium bolts placed in one column. In order to assess the effect of the different amount of by-pass and bearing load on the failure mode, each specimen type was produced in two versions: narrow (N) with a width of 36 mm and wide (W) with a width of 44 mm. The impact of clamping was studied on the single-shear countersunk wide specimens, which were tested at two different pretension levels: finger-tight (FT) ≈ 1 Nm and the pretension level (PRE) ≈ 6.5 Nm. All other specimens were clamped with finger-tight pretension. The parts were made of the following materials:

- CFRP laminates HTA6376, layup $[(+45/-45/0/90)_{s2}]_s$
- Aluminium plate, AA7475-T76
- Fasteners Ti-6Al-4V-STA (AMS 4965)

Besides the above, variants of both the protruding and the countersunk single-shear wide specimens, were manufactured with local bolthole reinforcement (R). A technique was used where a substitution of the composite plies by thin metal foils is performed in the area surrounding the bolt hole [3, 4], see Fig. 3.1-1. Circular stainless steel reinforcement inserts of

two diameter sizes were inserted in holes, which were cut in the pre-preg material in advance, and co-cured together with the laminate with thin adhesive film inbetween.

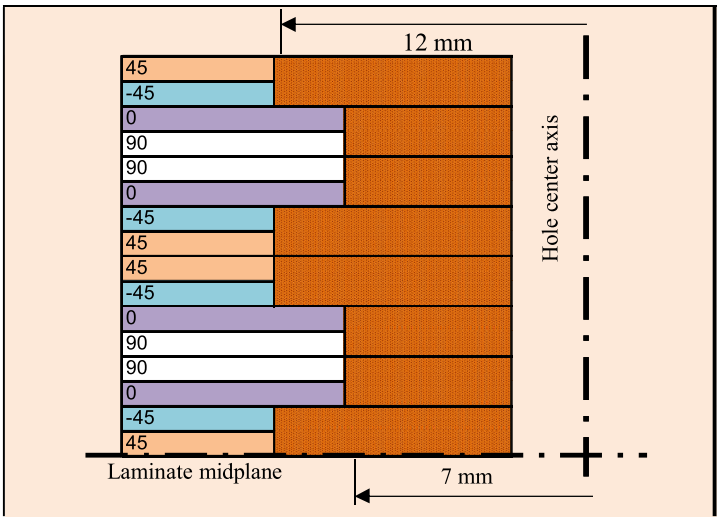

Figure 3.1-1. Reinforcement inserts dimensions.

Experimental procedure

The specimens were clamped at both ends and loaded to failure quasi-statically in a tensile machine. Measurements of the applied tensile force and cross head displacement were recorded continuously during the loading for all specimens. The final failure mode (net-section, bearing, bolt shear) and its position were noted. The typical failure modes are shown in Fig 3.1-2.

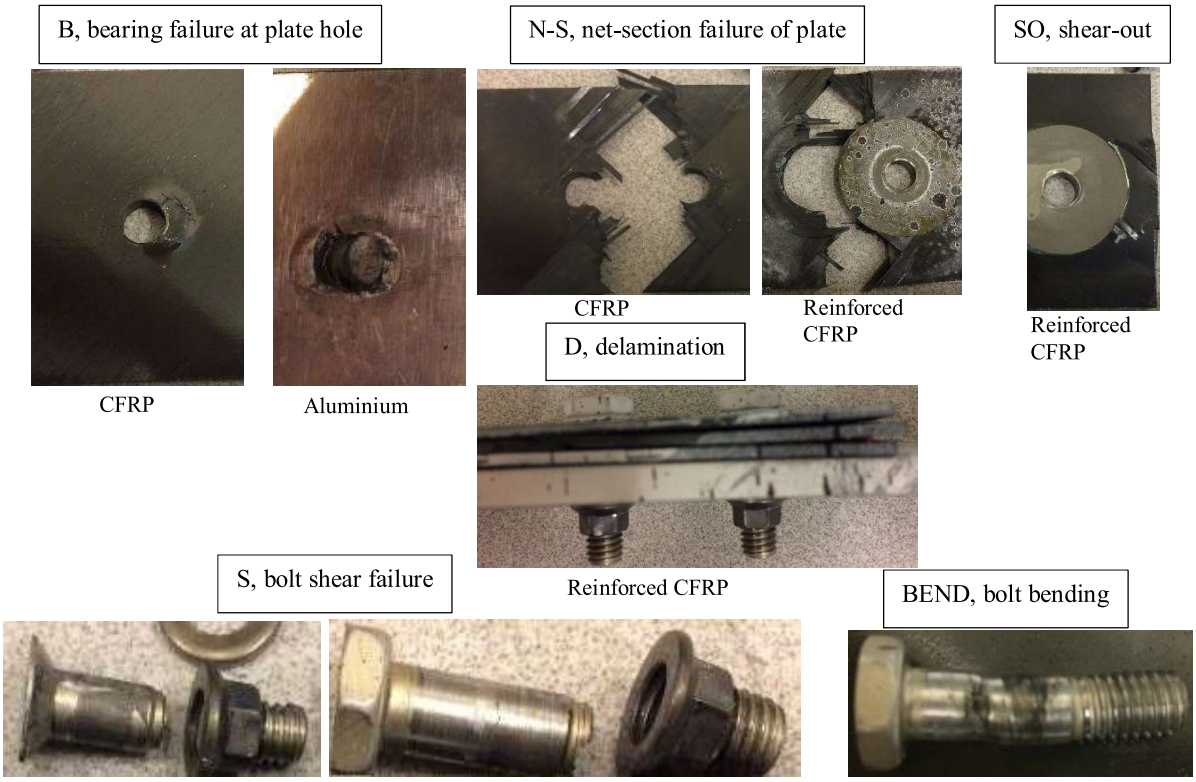

Figure 3.1-2. Typical failure modes.

Results

Figure 3.1-3 and 3.1-4 show, the force-grip displacement curves obtained by tests of double and single shear, protruding and countersunk bolt head specimens with wide and narrow plates, with and without the reinforcements.

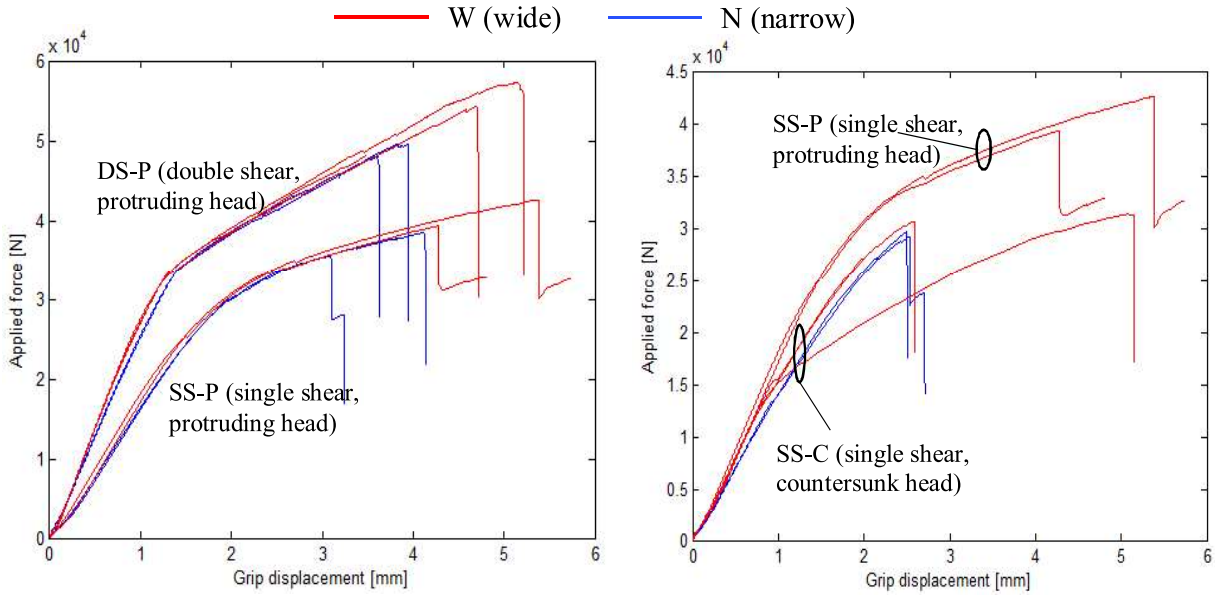

Figure 3.1-3. Force-displacement curves for wide and narrow protruding and countersunk bolt head specimens with finger tight pretension.

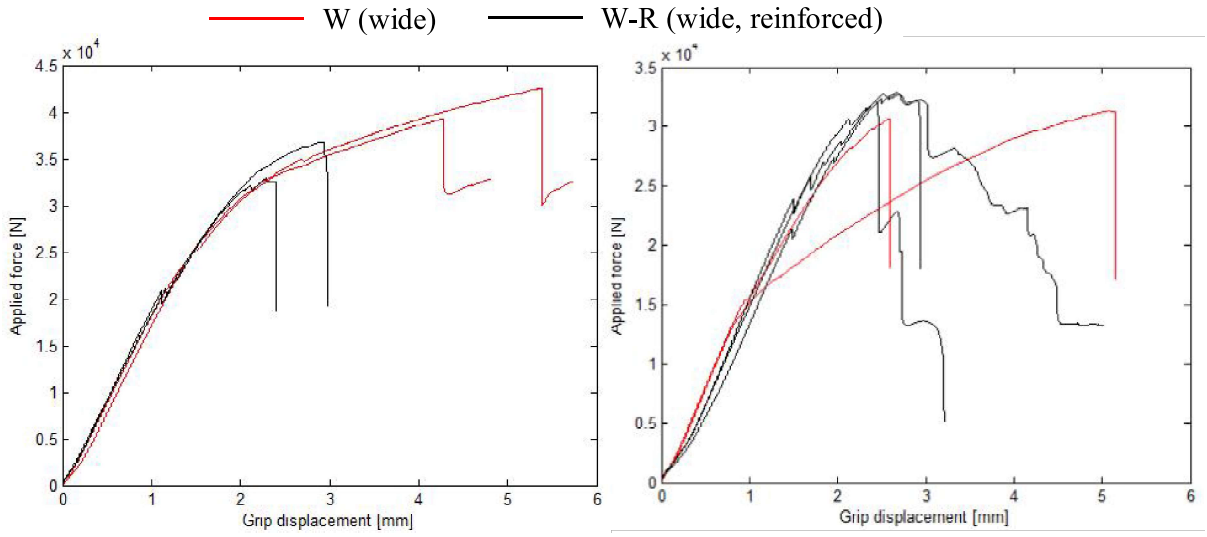

Figure 3.1-4. Force-displacement curves for wide, protruding (left) and countersunk (right) bolt head specimens, with and without reinforcements.

An example of a numerical simulation result is presented below. For details regarding the FE model and material modelling of CFRP refer to [2]. For metallic parts Abaqus ductile failure models are used. Figure 3.1-5 shows a comparison of the applied grip force-displacement response between the simulation and the test measurement, Fig. 3.1-6 shows the composite

damage and the equivalent plastic strain in the aluminium plate in the simulation, and Fig. 3.1-7 shows the borken test specimen.

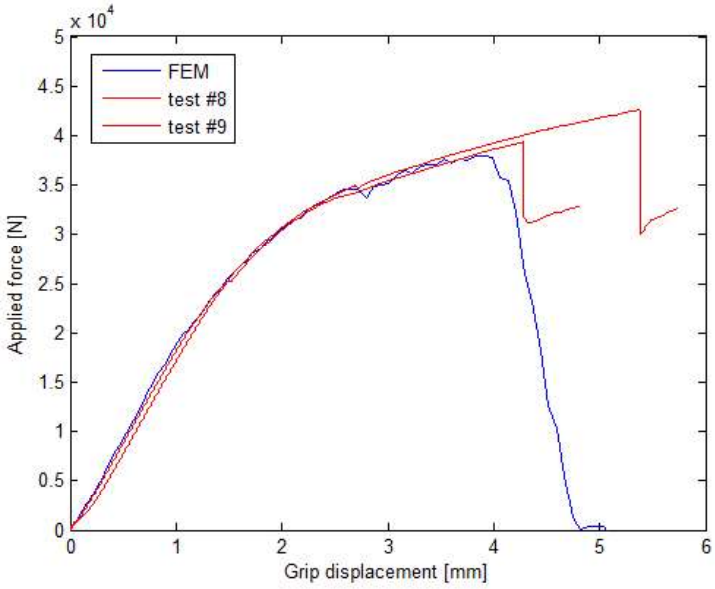

Figure 3.1-5. Force displacement curves for single shear specimen with protruding bolt head, test vs FEM.

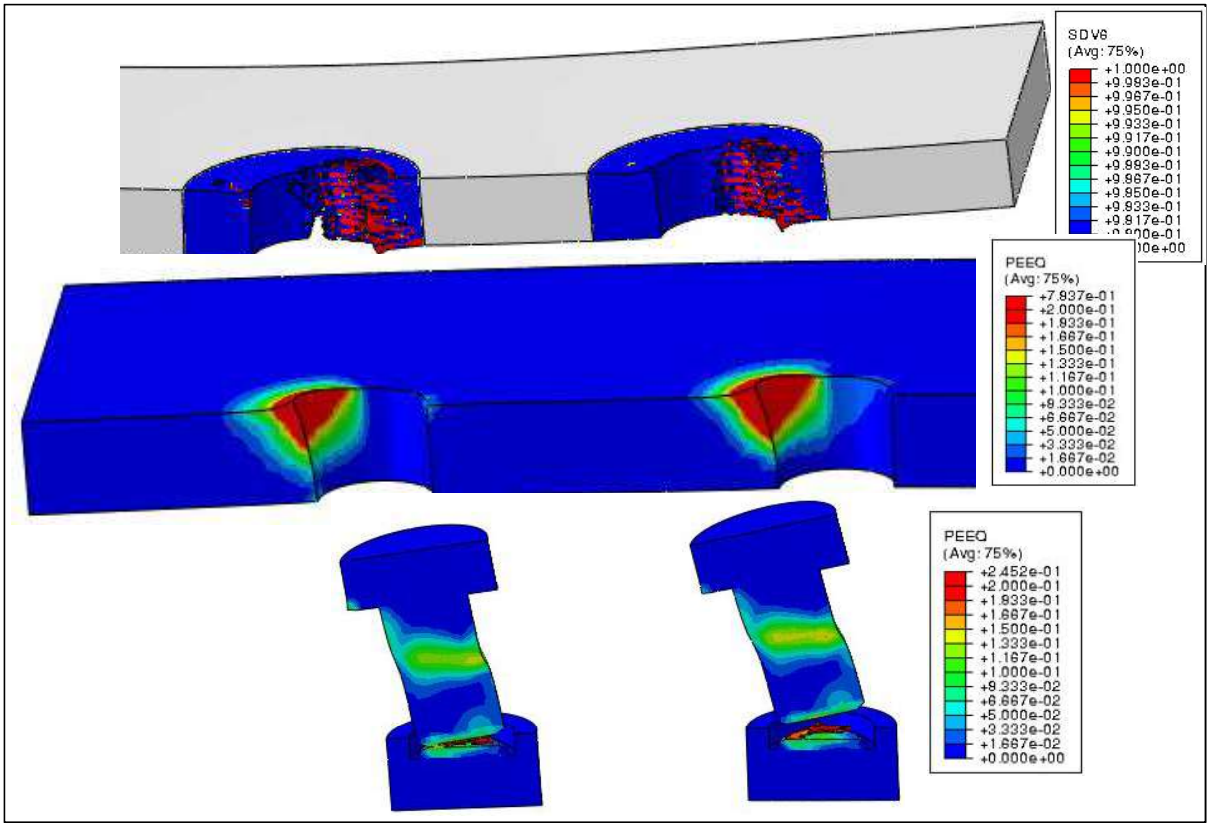

Figure 3.1-6. Compressive fibre damage (CFRP), equivalent plastic strain (Al and bolts) at failure load.

Figure 3.1-7. Broken test specimen.

Conclusions

As expected, the test results show that introduction of secondary bending and/or countersunk holes has a detrimental effect on the initiation of irreversible damage and on the failure load and failure mode of the joint. In all considered unreinforced joint configurations, the initial bearing damage takes place at the composite hole edge at a load level which is independent of the plate width. Pretension seems to have a delaying effect on the bearing damage initiation.

The damage progression and the final failure of the unreinforced joint depends on the joint configuration. Double shear joints failed in net-section mode, while in the single shear joints the bolts were bent/sheared off at the threaded sections in most cases. In both configurations, the bearing damage in the CFRP and the plastic deformation of the hole edge in the aluminium plates progressed prior to the failure.

The reinforced specimens experienced extensive delamination where after the load dropped from its maximum value. For more information about the reinforced composite holes see [4] and its references. Simulations were able to predict the initiation and progression of the bearing failure, the net/section failure and the bolt failure in the studied cases rather well. There are, however, a number of issues regarding the modelling of the failure that can be improved, see [2] for a more detailed discussion.

References

[1] Ireman T. Design of composite structures containing bolt holes and open holes,PhD dissertation thesis, KTH, 1999.

[2] Kapidzic Z, Ansell H, Schön J, Simonsson K. Quasi-static bearing failure of CFRP composite in biaxially loaded bolted joints. Compos Struct 2015;125:60–71.

[3] LN-029643. WP 22 LOCOMACHS Hålkantsförstärkning – Tillämpning Gripen.

[4] Akbarpour A, Hallström S. Metal reiforcement around fastener holes in composites. ECCM17-17th European Conference on Composite Materials, Munich, Germany, 2016.

3.2 Metal reinforcement around fastener holes in composites

Sahar Akbarpour, Stefan Hallström, KTH

Introduction

An effective way to improve the load bearing capacity of bolted joints in composites is to use local hole reinforcement with high-strength metals. KTH and SAAB have mutually developed a local hole reinforcement concept, schematically illustrated in Fig. 3.2-1.

(a) (b)

Figure 3.2-1. A specimen with a patched metal insert (a) and a schematic of the insert geometry (b)

The concept uses inserts built from stacked metal patches at the locations of the holes in order to improve the bearing strength of the composite. The core of the concept is the idea to separate the bearing stress problem from the hybrid metal-composite joint problem and handle the two at different interfaces rather than at the same. In the way it is implemented the concept also provides a number of other benefits. One is the great potential for weight saving in cases where the bearing strength drives the laminate thickness. In addition, the presented concept enables clamping pressure by the fasteners and thereby joints can also partly carry load by friction. Finally, layer-wise integration of the inserts in the prepreg laminates during curing, and simpler drilling operations compared to co-drilling of metal-composite interfaces are additional advantages.

After doing some initial tests and a parameter study, some specimens with optimized stacked patch inserts were designed for pin-loaded and open-hole tensile tests within the EU project Locomachs. In another test series, some double-bolt joints were assessed in single and double-shear tests as part of the RASK project. In addition to experimental work, finite element analysis has been performed in order to investigate the local stress states and the failure mechanisms.

The insert concept could potentially also enhance the efficiency of multi-row bolted joints. A joint with higher efficiency is generally defined as a joint that carries more load without adding considerable weight. Considering multi-row bolted joints, the efficiency is not only governed by the bearing strength but also by the bypass load between the fastener rows. Increasing the efficiency of joints in composite laminates would generally increase the efficiency of the whole composite material since the thickness of composite material often is driven by the joint strength.

Previous research activities [1-4] have reported results demonstrating the advantageous influence of titanium hybridization on specific characteristics of CFRP-materials. It was demonstrated that the use of hybrid laminates with 20% titanium content increased the specific tensile strength of a three-row bolted joint by 32% when compared to that of a CFRP laminate. The specific bearing strength of a hybrid joint with 50% titanium content at the bearing region was 29% higher than that of a monolithic CFRP joint.

In the current research activity, the metal inserts have so far been made of stainless steel, mainly due to strength and cost considerations. The relatively high density and coefficient of thermal expansion (CTE) are disadvantages with the stainless steel. High strength titanium alloy is considered to be the most suitable choice especially for high-temperature applications because of its relatively high strength and low CTE. Being electrochemically compatible with carbon material and showing a relatively low mismatch of its stiffness and strain to failure are other advantages with titanium alloys [1-4].

Experimental study

Pin-loaded and open-hole tensile tests

Some specimens with optimized inserts were designed. The details of the materials, specimen geometries and manufacturing processes are presented in [5]. Two insert configurations were optimized for good and deliberately poor performance. The "Good" and "poor" configurations had identical insert geometry (Figure 3.2-2(a)) but different stacking sequences. (In the poor case the stacking sequence was simply turned 90° from the good case.) In addition to the good and poor configuration, three other insert configurations were designed by varying the stacking of the metal patches and the prepreg plies. These configurations were made from fewer metal patches and labeled as I5, I6 and I7, shown schematically in Figure 3.2-2(b), (c) and (d).

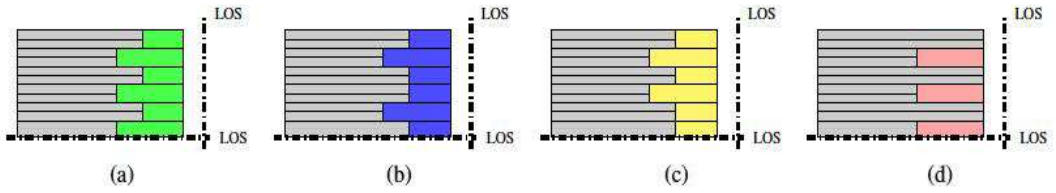

Figure 3.2-2.Insert configurations of “good” and “poor” cases (a), I5 (b), I6 (c) and I7 (d)

- ***Pin-loaded tests***

The pin-loaded test setup is shown in Figure 3.2-3. The results from the pin-loaded tests were in general strikingly consistent with very low scatter as shown in Figure 3.2-4. The optimized good case showed 60% strength improvement compared to its reference while the "poor" case showed only 12% improvement of the ultimate load. The pin-loaded test results for I5, I6 and I7 configurations showed about 50% improvement in bearing strength as shown in Figure 3.2-4. The "good" case (and also I5, I6 and I7) showed bearing failure and the "poor" case showed premature failure as shown in Figure 3.2-5.

Figure 3.2-3. Test setup for a pin-loaded specimens

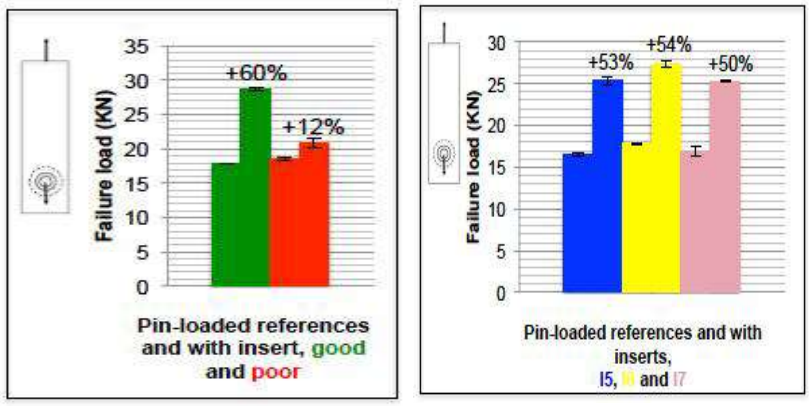

(a) (b)

Figure 3.2-4. Bearing failure loads of the good and poor cases (a), I5, I6 and I7 (b)

(a) (b)

Figure 3.2-5. Bearing failure of the good (a) and premature failure of the poor (b) configurations

- ***Open-hole tensile tests***

Open-hole tensile tests measure the strength of the finger-joint between the metal patches and the composite and also indicate the amount of by-pass load that can be transferred around the hole. The open-hole test setup is shown in Figure 3.2-6. The tensile strength of the good configuration came out 13% lower than for the reference case as shown in Figure 3.2-7. The tensile strength of I5 was considerably higher while I6 was slightly lower than for the reference case. None of the configurations were however designed for good performance in open-hole tensile tests.

Figure 3.2-6. Test setup for open-hole tensile tests

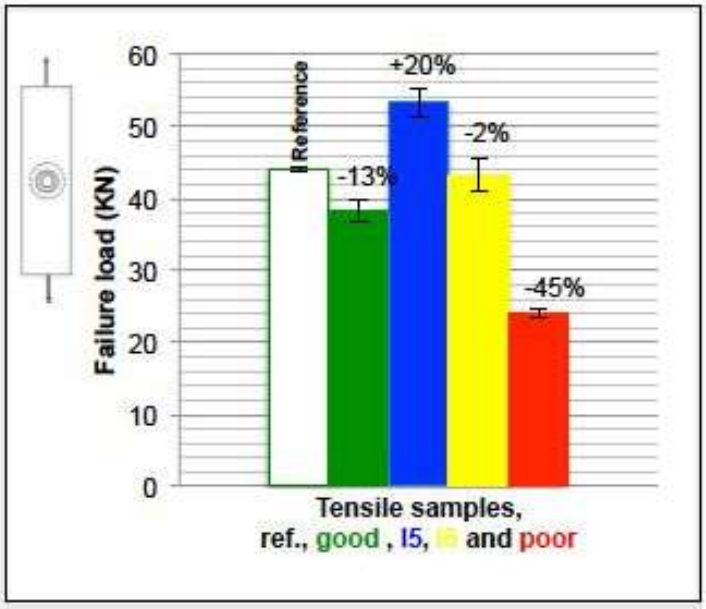

Figure 3.2-7. Open-hole tensile results for optimized configurations

Single-shear and double-shear tests

Two specimens with the I5 insert configuration were designed and tested in hybrid bolted joint tests, either in single or double shear surfaces. Tests were also performed on two thicker specimens containing of 32 prepreg plies, an insert configuration labeled as I10 (Figure 8 (b)). Two corresponding reference specimens were also tested for each insert configuration.

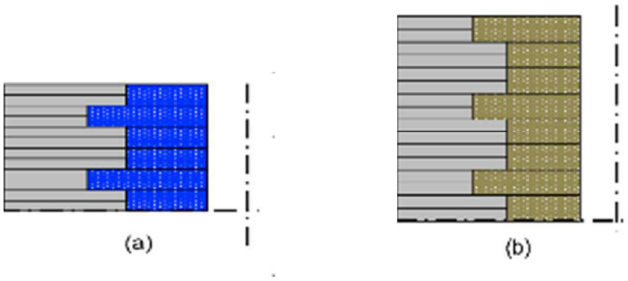

Figure 3.2-8. Insert configurations of I5 (a) and I10 (b)

- ***Single-shear tests***

The single-shear test setup is shown in Figure 3.2-9. Based on different methods for identifying the failure point on the load-displacement graphs, the failure load of I5 and I10 were 10-30%, and 15-25% higher than for the reference cases, respectively. The specimens with the I5 insert configuration showed net section failure while bearing failure occurred for the specimens with I10 insert configuration (Figure 3.2-10).

Figure 3.2-9. Test setup for single-shear test

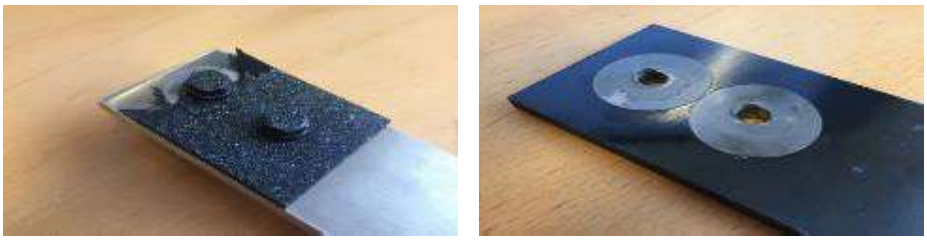

Figure 3.2-10. Net-section failure of specimen with I5 (a) and I10 (b) insert configuration

- ***Double-shear tests***

The load-displacement graphs are shown for one specimen with washer and two reference specimens in Figure 3.2-11 (because of some problems only one test with inserts could be performed properly).

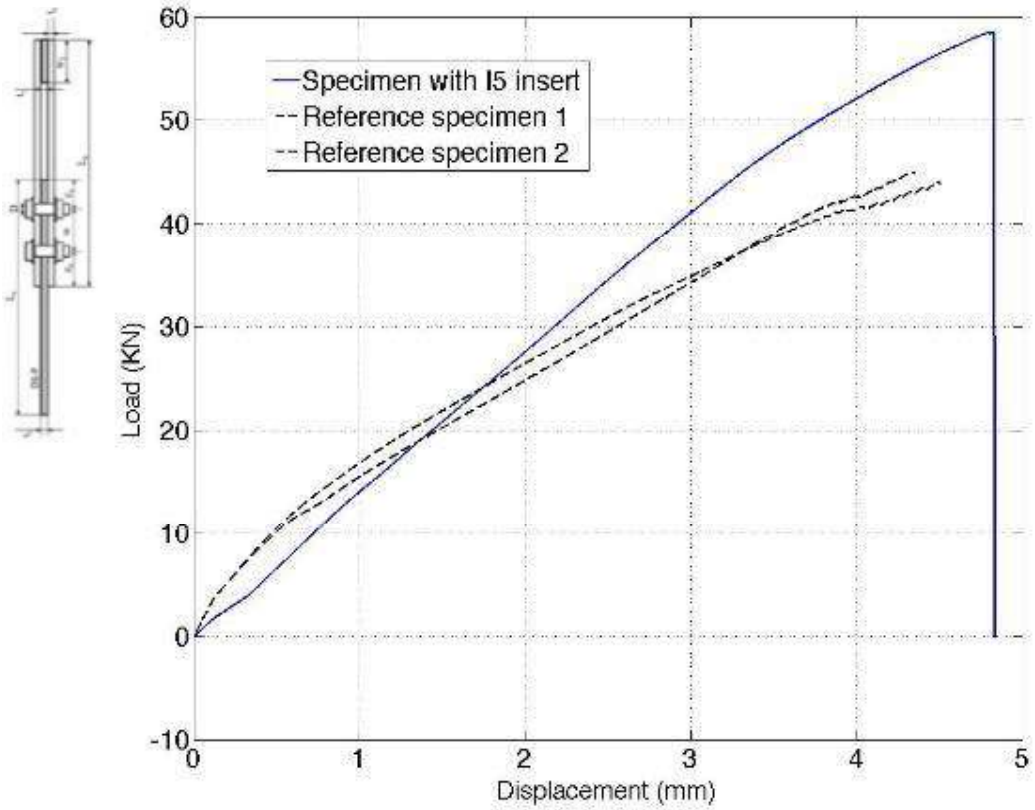

Figure 3.2-11. Load-displacement graphs of two reference specimens and one specimen with the I5 insert configuration

Finite element analysis

2-dimensional FE models were used to analyze the stresses at the multi-material edges of tensile specimens with strip inserts, using Ansys 14.0. In the neighborhood of the multi-material corners, where there are high stress concentrations due to the elastic mismatch, a very fine mesh was used (Figure 3.2-12). The applied mechanical load was introduced as predefined displacement at the specimen ends and thermal load was also applied to simulate residual stresses from the curing process.

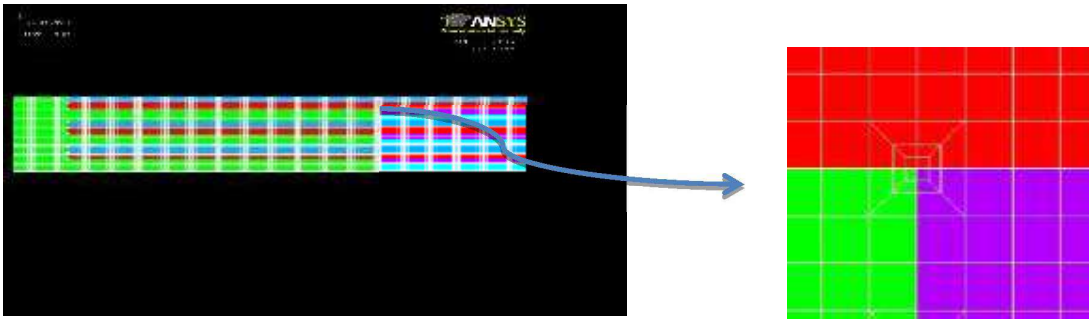

Figure 3.2-12. A 2D FE model of a specimen with a strip insert

Conclusions

Local hole reinforcement of composite laminates with inserts made of stacked metal patches is an effective way to improve load bearing capability of bolted joints. In the research work, a number of specimens with different insert configurations were designed and tested and several of them showed more than 50% strength improvement in pin-loaded tests. In addition to the bearing strength the by-pass load is also an essential parameter related to the load capacity of multi-row bolted joints. The by-pass strength of specimens with inserts was also examined through open-hole tensile tests. One insert configuration showed 50% and 20% improvement in bearing and by-pass strength respectively. It also came out considerably stronger than the corresponding references in single and double-shear tests. In fact, the specimens with inserts showed similar failure loads as 25% thicker specimens without inserts. It is clear that proper implementation of metal inserts through tailored stacking of patches at the holes of composite laminates can improve the strength of bolted-joints considerably. The efficiency of joints in composites could thus be improved significantly and thereby reduce the weight of composite parts and even structures, since their thickness in many cases is driven by requirements on the joints. Further analysis and optimization activities are foreseen to bring the concept closer to industrial implementation.

References

[1] A. Fink, P.P. Camanho, and B. Kolesnikov. Hybrid titanium composite material improving composite structure coupling. *European conference on spacecraft structures, Materials and Mechanical Testing,* 2005

[2] B. Kolesnikov, L. Herbeck, and A. Fink. CFRP/titanium hybrid material for improving composite bolted joints. *Composite Structures,* 83:368-380, 2008

[3] P.P. Camanho, A. Fink, A. Obst, and S. Pimenta. Hybrid titanium-CFRP laminates for high-performance bolted joints. *Composites:Part A,* 40:1826-1837, 2009

[4] A. Fink, P.P. Camanho, J.M. Andrés, E. Pfeiffer, and A. Obst. Hybrid CFRP/titanium bolted joints: Performance assessment and application to a spacecraft payload adaptor. *Composite Science and Technology,* 70:305-317, 2010

[5] S. Akbarpour and S. Hallström. Metal reinforcement around fastener holes in composites. *European Conference on Composite Materials*, 2016

3.3 Study of 3D fibre reinforcement in noodles in composite T-joints

Tomas Ekermann and Stefan Hallström, KTH Royal Institute of Technology

When joining two composite plates, e.g. skin and stiffener, usually a T-joint is used. The horizontal part is here referred to as the skin and the vertical part is called the flange. In order to comply with a given radius between the two parts the cavity between them is filled with a noodle (
Figure 3.3-2). When the T-joint is subjected to external loading the load is transferred from the flange into the skin through the noodle area and in some load cases the noodle-laminate interfaces tend to become critical for the strength. The performance of the T-joint is therefore heavily dependent on the noodle area and potentially also on the noodle properties, although (and partly because) the noodle itself is not a primary load-carrying part of the junction. In addition to the in-service loading there might also be significant influence from residual stresses related to shrinkage during curing and cooling of the T-joint, where the temperature is decreased from 180°C. Since the laminates surrounding the noodle are relatively stiff in-plane they constitute constraints on the noodle when it contracts due to the temperature drop. This may create residual stresses in the noodle and potentially reduce the strength of the T-joint.

In this project an investigation is undertaken to study what influence the directions of the reinforcing fibres in the noodle have on the pull-out strength of the T-joint. It is realised though mechanical pull-off tests performed on T-joints with different configurations of 3D-woven noodles, having different amount of fibres in the three principal directions (a visualisation of one 3D-woven noodle is seen in
Figure 3.3-2). The 3D-woven noodles are manufactured by the principle of 3D-weaving developed by Khokar [1], where a matrix of warp yarns are interlaced with two perpendicular (horizontal and vertical) sets of weft yarns. As a reference T-joints with a conventional 1D-reinforced UD-noodle are also tested. Furthermore, FE-simulations are performed on T-joints with a variety of noodles, including the conventional UD-noodle, 3D-woven noodles and homogenized UD-noodles with the fibres aligned transverse to the noodle extension.

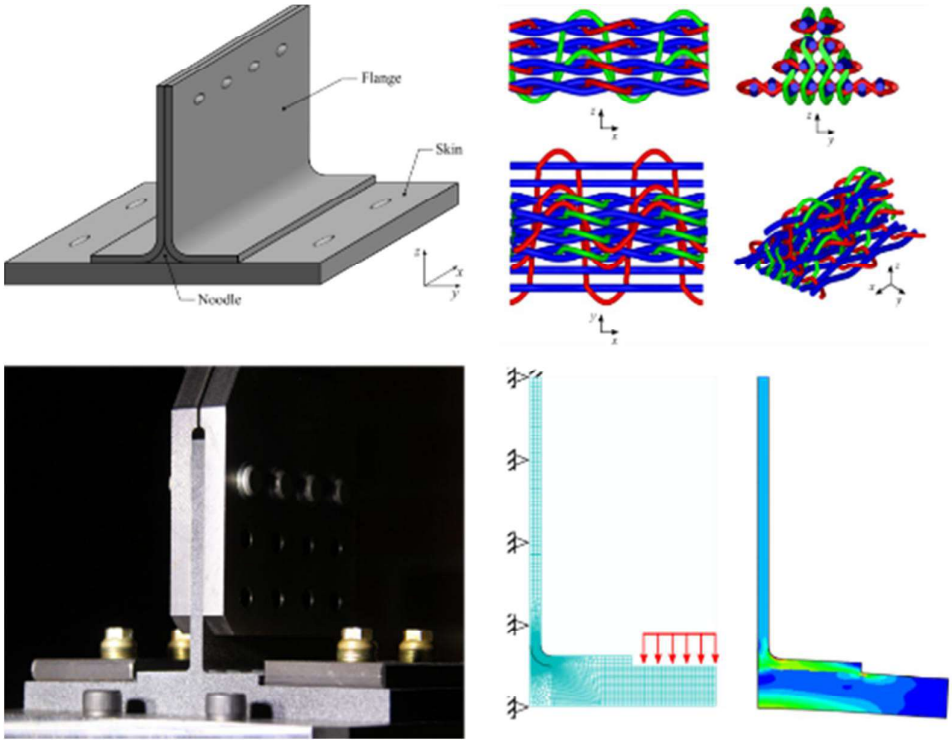

Figure 3.3-2 Upper left: Principle sketch of the T-joint where the individual parts have been identified. Upper right: A model of a 3D-woven noodle created in the textile modelling software TexGen. Lower left: Set-up of the pull-off test. Lower right: FE-model with loads and boundary conditions, and deformed with maximum the principal stressed indicated.

[1] N. Khokar, *3D-weaving: Theory and Practice*, Journal of the Textile Institute, 2001, 92

4 THERMAL MECHANICAL FATIGUE OF SUPERALLOYS

4.1 Modelling the crack initiation and propagation in a gas turbine disc alloy under thermomechanical fatigue conditions

Daniel Leidermark
Division of Solid Mechanics, Linköping University, Sweden

In order to reach a more sustainable energy and resource usage system for the future, in which gas turbines (for propulsion and power generation) by necessity will continue to play a central role, there is a strong need for making these machines more efficient than today, which calls for higher combustion temperatures. In this context, more efficient cooling, material characterisation and life assessment models are of huge importance. With this in the back Rolls-Royce (UK) initiated the EU-funded research project: Development of experimental techniques and predictive tools to characterise thermomechanical fatigue behaviour and damage mechanisms in two nickel-base superalloys (DevTMF). This project will be ongoing

from 2016 through 2019, with the international team comprised of Linköping University (Swe), University of Nottingham (UK) and Swansea University (UK), which will perform the work in the project.

The aim of the project is to investigate, characterise and model the thermomechanical fatigue (TMF) crack growth behaviour of the relative coarse-grained disc alloy RR1000. Furthermore, to be able to properly predict the crack growth behaviour in the material under TMF load conditions, the constitutive and crack initiation behaviour need to be fully understood, quantified and modelled. Note that the project has just recently started and an outline of the upcoming work to be performed within the project is given below.

On the constitutive side, a macroscopic small-scale yielding model employing the von Mises equivalent stress with the kinematic Ohno-Wang backstress description [1] and a saturated isotropic cyclic softening will be used. In addition, during the dwell times of the TMF cycle creep deformation (stress relaxation) will occur. The aim is to model the creep by use of the Norton-Odqvist viscoplastic dissipation potential in cooperation with a Kachanov creep damage description [2]. Creep is to be considered active continuously during the entire loading, whereas plasticity will only be active when above the yield limit.

In an industrial application, it is very demanding to perform finite element simulations of every cycle in the TMF loading sequence until failure. Hence, an approach to minimise the computational time is to perform some kind of cycle jumping procedure. Either a parameter modification or extrapolation method can be adopted to generate an efficient evaluation procedure of the stress/strain state, which in turn will give a sufficient crack initiation and propagation behaviour. An evaluation of cycle jumping procedure is undertaken within the project, where a modification and an extrapolation method are compared.

Before a crack starts to propagate and grow, it will initiate somewhere. The initiation location is usually in highly stressed/strained areas, where the local damage has reached a critical level so that material separation is imminent. The local damage can be attributed by flaws, surface roughness, oxidation, fretting, impact damage and/or local plasticity. Based on inspiration from real micro mechanisms, a local continuum damage approach will be employed to quantify the number of cycles to crack initiation and the location of the growing crack, see e.g. [3]. This local damage is to be related to the surface damage, as cracks are prone to nucleate at the surface.

The crack propagation modelling at these conditions will be defined by decoupling of time independent fatigue and time dependent creep crack growth, and their individual responses are summed together in a total crack extension based on the work of Bouvard [4]. Oxidisation will have an effect on the fatigue crack growth. Oxide layer thickening on the exposed crack surface may, for example, retard crack growth rates due to the associated increase in the opening threshold. Conversely, oxygen diffusion into the bulk material ahead of the crack tip can cause embrittlement, thereby accelerating the crack growth. It has from previous research been observed that the oxidation and crack closure play an important role in disc alloys [5]. This needs to be handled in a proper manner.

All of the above mentioned modelling work will also be accompanied by a vast experimental testing program. Testing at high temperature conditions, especially at TMF loading conditions, is usually conducted with an induction coil, and this generates a problem when the growing

crack is monitored with the commonly used potential drop (PD) technique. Hence, the testing need to be "paused" when performing the PD-measurements in each cycle, as the induction field cancels the electrical measure as PD uses. Standardisation and practical approaches will be investigated and evaluated.

References

[1] Ohno N, Wang JD. Kinematic hardening rules with critical state of dynamic recovery, Part I: Formulation and basic features for ratchetting behavior. International Journal of Plasticity. 1993;9:375–390.

[2] Kachanov LM. On the time to rupture under creep conditions. Izv. Acad. Nauk SSSR. OTN. 1958;8:26-31.

[3] Jiang Y. Fatigue criterion for general multiaxial loading. Fatigue and Fracture of Engineering Materials and Structures. 2000;23:19–32.

[4] Bouvard JL, Gallerneau F, Paulmier P, Chaboche JL. A phenomenological model to predict the crack growth in single crystal superalloys at high temperature. International Journal of Fatigue. 2012;38:130–143.

[5] Storgärds E, Simonsson K, Sjöström S. Three-dimensional crack growth modelling of a Ni-based superalloy at elevated temperature and sustained loading. Theoretical and Applied Fracture Mechanics. 2016;81:2-10.

ACKNOWLEDGEMENTS

This editorial work was supported by Saab AB. The editor is also indepted to the following individuals who helped to write this review:

Zlatan Kapidzic	Saab AB	(Section: 2.3, 2.4, 2.5, 2.7, 3.1)
Martin Ekström	Saab AB	(Section: 2.1)
Rikard Rentmeester	Saab AB	(Section: 2.7)
Magnus Kahlin	Saab AB/LiU	(Section: 2.10)
Björn Fredriksson	Saab AB	(Section: 2.2)
Börje Andersson	BARE	(Section: 2.8)
Anders Klarbring	LiU	(Section: 2.9)
Ulf Edlund	LiU	(Section: 2.9)
Bo Torstenfelt	LiU	(Section: 2.9)
Johan Moverare	LiU	(Section: 2.10, 3.1)
Daniel Leidermark	LiU	(Section: 4.1)
Stefan Hallström	KTH	(Section: 3.2, 3.3)
Tomas Ekermann	KTH	(Section: 3.3)
Sahar Akbarpour	KTH	(Section: 3.2)
Enna Arasto	VTT	(Sections: 2.6)